ELSEVIER

Coordination Chemistry Reviews
178–180 (1998) 1573–1614

COORDINATION CHEMISTRY REVIEWS

Iron–sulfur clusters and their electronic and magnetic properties

Jean-Marie Mouesca *, Bernard Lamotte

Département de Recherche Fondamentale sur la Matière Condensée, SCIB / SCPM, C.E.A. Grenoble, 17 rue des Martyrs, 38054 cedex 9 Grenoble, France

Received 13 February 1998; received in revised form 28 April 1998; accepted 21 May 1998

Contents

Abstract

Iron–sulfur clusters of diverse nuclearities constitute the active sites of a large and prominent family of metalloproteins which play essential roles in all living organisms, such as in electron transfer chains, reduction catalysis, photosynthesis, the respiratory chain and nitrogen fixation. This review is devoted to the presentation of the current state of understanding of their

* Corresponding author. Tel: 0033 4 76 88 41 36; Fax: 0033 4 76 88 41 36;
e-mail: mouesca@drfmc.ceng.cea.fr

PII S0010-8545(98)00155-6

electronic and magnetic properties, which is here derived from their Mössbauer, EPR and ENDOR spectroscopic properties. These techniques constitute fine tools for characterization and provide knowledge of the different oxidation states of these proteins, although our interest here will be mainly centered on the $[4Fe\text{–}4S^*]^{n+}$ clusters (with $n=1$–3). A qualitative physical model involving the competing magnetic interactions in these clusters is discussed. Moreover, this article contains new developments on two more specialized subjects:

(1) some quantitative consequences of an already published theory of the g-tensors of $[4Fe\text{–}4S^*]^{n+}$ clusters ($n=1,3$) will be derived in Section 3;

(2) a model permitting the rationalization, from very simple ingredients and formulae, of the redox potentials of a whole set of known synthetic redox clusters (with 1, 2, 3, 4 and 6 iron atoms) will be presented in the final Section 6.

1. Introduction: the iron–sulfur proteins

Many different kinds of metal clusters are presently known, the properties of which have been investigated by scientists working within a range of different fields. An especially dynamic area of research is that of bioinorganic chemistry, which has emerged during the last 10 years as a field at the crossroads of chemistry, biology and even physics (due, as we will see, to the special interest of their electronic and magnetic properties). A wide variety of metalloproteins and metalloenzymes have one, two or more, transition metal(s) present in their so-called active sites, most often the site of electron transfer or redox catalysis. Among these enzymes, the iron–sulfur (Fe–S) proteins constitute a prominent category which is interesting in many aspects [1,2]. Since their discovery in the mid-1960s, almost two hundred have been identified and characterized, and the biochemical knowledge gained has grown exponentially. They are ubiquitous in nature, present in the most primitive monocellular organisms as well as in plant cells and in Man. Many of these proteins have been called ferredoxins (Fds), since they contain iron and generally exhibit redox properties. They frequently mediate electron transfer in fundamental processes such as bacterial and plant photosynthesis or the mitochondrial respiratory chain, either as soluble proteins in the cytoplasm or as part of membrane bound complexes. But there are also some especially important iron–sulfur enzymes which play other prominent roles like nitrogenases in nitrogen fixation or hydrogenases permitting the reduction of protons to form hydrogen. Moreover, it has been established during the last 5 years that there further exists several categories of iron–sulfur proteins which are "non-classical" in the sense that they possess non-redox activities. Rather, these last proteins function as sensors of iron or oxygen, or as gene regulators, thus increasing their functional diversity.

After a short discussion of the many iron–sulfur clusters presently known, our purpose in this review is to focus on their electronic and magnetic properties. In effect, magnetism stands as their most fundamental property and provides us with an indispensable means of characterization which in itself has given rise to quite interesting, complex and original problems of molecular magnetism. Special emphasis will be put for this purpose on the spectroscopic methods of Mössbauer and of electron magnetic resonance (electronic paramagnetic resonance, and electron

nuclear double resonance: EPR and ENDOR, respectively), which have proved to be essential tools for the study of proteins, their active sites and corresponding synthetic analogs. These methods are fine tools of characterization for the different oxidation states of iron–sulphur proteins, and therefore of the subtle modifications occuring around their active sites. Remarkably detailed knowledge of their electronic structures can be gained, reflecting the keen nature of these methods.

In the text that follows, we will therefore present and discuss successively:

(1) The magnetic properties of the clusters as a function of their oxidation states; our interest here focussing mainly on clusters containing four iron atoms. These states will be at first introduced from the results of Mössbauer studies as published in the literature. We will then present insights provided by EPR and ENDOR spectroscopies, restricting our discussion mainly to those results obtained in our laboratory. Then we will consider how we may rationalize and understand, with our present knowledge, all these data through the use of a physical model involving the different magnetic interactions in competition. This part of the review (Sections 2–4) constitutes, therefore, a summary of the literature and of our own contributions to the field. We will, however, present two more detailed and original contributions:

(2) The first one, imbedded in Section 3, directly related to the spectroscopic and magnetic properties of the clusters, exposes further developments of the *g*-tensors theory that we have recently published [3];

(3) The second one (Section 6), dealing with redox properties, proposes a simple model encompassing in one formula the redox potentials of the whole family of known synthetic redox clusters.

Let us add that we have chosen to limit the scope of this text to the description of spectroscopic and magnetic properties of the clusters, by dealing only with the analyzes of Mössbauer, EPR and ENDOR studies. The reason for this is that these techniques probe magnetic ground states as they are operated at temperatures close to that of liquid helium. We have, therefore, deliberately excluded here any discussion relative to NMR studies (liquid or solid-state), whose interpretation is made more complicated as they are performed around room temperature and, therefore, involve also the magnetic excited states of the clusters.

2. Iron–sulfur active sites of proteins and their synthetic model analogs

Fig. 1 presents a variety of clusters already characterized as being active sites of some Fe–S proteins. It must be pointed out that, while the majority of these proteins contain only one of the active sites described in Fig. 1, a rather large number of Fe–S proteins contain two or more, or even possess, in addition, a different prosthetic group. In Fig. 1(a) the building block common to (almost) all of these clusters is represented, i.e. one iron atom tetrahedrally ligated by four sulfur atoms. Exceptions are rare, but should be mentioned, for instance when one iron ion turns out to be bound to an oxygen [4], or to two nitrogen-based ligands [5,6].

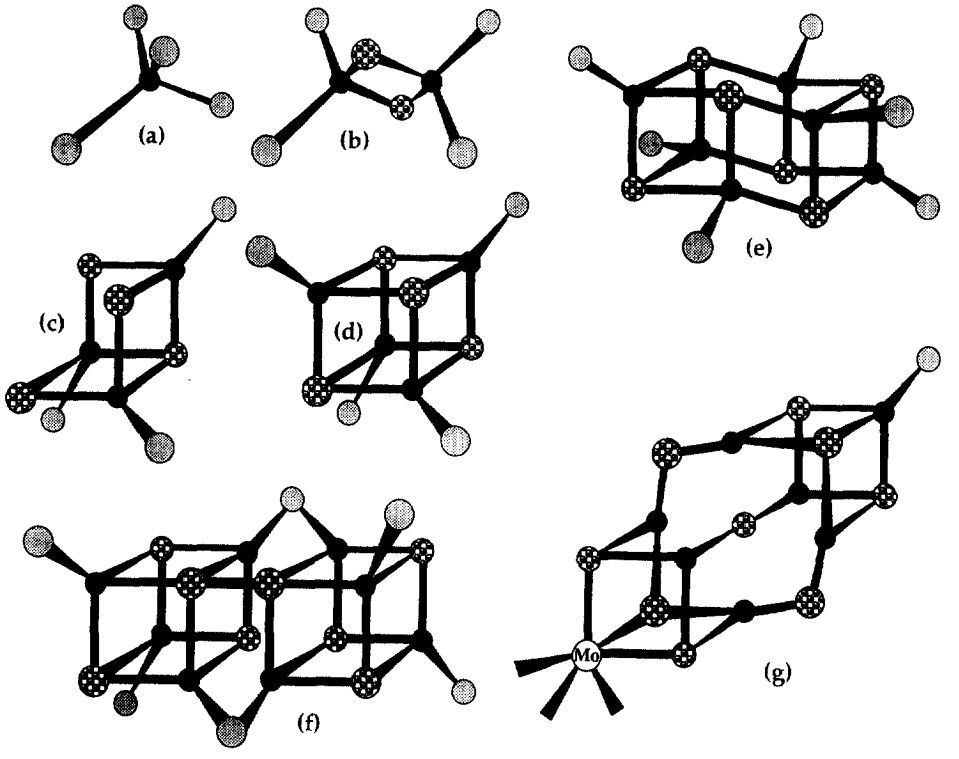

Fig. 1. Schematic views of the different active sites known for iron–sulfur proteins: with (a) one, (b) two, (c) three, (d) four, and (e) six iron atoms. The two iron–sulfur clusters of nitrogenase: (f) the "center P", and (g) the FeMo cofactor. Black circles stand for Fe atoms, grey ones for cysteinyl S, and spotted ones for inorganic S*, atoms.

Among the first issues one has to face when dealing with these Fe–S clusters is the determination of the formal charges (and therefore spin states) of each iron ion and, as a second step, of the way in which these spins are coupled altogether, giving rise to the global magnetic properties of these clusters. This problem, and especially the first part of it, has essentially been tackled by Mössbauer spectroscopy. In effect, this method yields two basic parameters which form the basis of the identification of the iron oxidation states in Fe–S clusters. These are the isomer shift "δ" and the quadrupole splitting, "ΔE_Q". The first of these, for which the main results are reported in Table 1, appears as the most important for this purpose, and will discussed at length now.

In the simplest case of the rubredoxins (Rds) where the building-block constitutes per se the active site of these particular proteins [cf Fig. 1(a)], the sulfur atoms belong to four cystein amino acids of the protein backbone. The iron atom is Fe^{3+} in the oxidized state, with a value of δ equal to 0.25 mm s^{-1} [1,7], which is thus characteristic of a high-spin ferric iron ion surrounded by four tetrahedrally coordinated sulfur ligands. In the reduced state of the protein, δ is measured around

Table 1
Isomer shifts δ (mm s^{-1}) of iron ions in their redox states 2+, 2.5+ and 3+ as measured for some typical 1Fe–, 2Fe–, 3Fe– and 4Fe–Sulfur systems

δ (mm s^{-1})	Fe^{2+}	$Fe^{2.5+}$	Fe^{3+}	Total spin
$[Fe]^{3+}$	—	—	1×0.25	5/2
$[Fe]^{2+}$	1×0.70	—	—	2
$[2Fe–2S^*]^{2+}$	—	—	2×0.27	0
$[2Fe–2S^*]^{1+}$	1×0.72	—	1×0.30	1/2
$[3Fe–4S^*]^{1+}$	—	—	3×0.27	1/2
$[3Fe–4S^*]^{0}$	—	2×0.46	1×0.32	2
$[4Fe–4S^*]^{1+}$	2×0.60	2×0.50	—	1/2, 3/2
$[4Fe–4S^*]^{2+}$	—	4×0.45	—	0
$[4Fe–4S^*]^{3+}$	—	2×0.40	2×0.30	1/2

0.70 mm s^{-1}, which will be thus considered as characteristic of a high-spin ferrous ion in the same coordination and chemical environment [1,7].

We can see in Fig. 1(b) the [2Fe–2S*] dimer, a relatively frequent active site which can be found, for instance, in ferredoxins (Fds) belonging to the photosynthetic electron transfer chain of plant chloroplasts. The iron atoms are bridged altogether by inorganic μ_2-sulfides (of formal charge S^{2-} noted S*, in a core notation [*m*Fe–*n*S*]) and further ligated to two sulfur atoms of cystein residues. Both iron atoms are Fe^{3+} in the oxidized state $[2Fe–2S^*]^{2+}$, as shown by Mössbauer since two (almost identical) ferric ions are identified, having $\delta\approx0.27$ mm s^{-1}. The reduced state $[2Fe–2S^*]^{1+}$ corresponds to a *mixed-valence state* comprising one Fe^{2+} and one Fe^{3+}, again as easily deduced from Mössbauer spectroscopy since the ferric ($\delta\approx0.30$ mm s^{-1}) and ferrous ($\delta\approx0.72$ mm s^{-1}) components are in that system are clearly identifiable [1]. For a review of mixed valence systems in chemistry, physics and biology, the reader is refered to Refs. [8,9].

The most common and most representative active site is constituted by the [4Fe–4S*] cluster [Fig. 1(d)]. In this case, each iron atom is approximately tetrahedrally coordinated to three inorganic μ_3-sulfur ions and to one (external) sulfur of a cystein amino acid. This cluster adopts a *cubane-analogue* shape, iron and sulfur atoms alternating on the cubane-analogue summits. It can also be viewed as two interpenetrating tetrahedra made up of iron and sulfur atoms, the second tetrahedron being larger than the first one, due to the larger size of the sulfur radii with respect to those of the iron ions. Three different redox states, i.e. $[4Fe–4S^*]^{3+}$, $[4Fe–4S^*]^{2+}$ and $[4Fe–4S^*]^{1+}$, have been identified in proteins. The 2+/1+ redox couple is involved in ferredoxins (where one can find sometimes two clusters of this type, symmetrically disposed), but also in enzymes like reductases, and hydrogenases, as well as in photosystem I. By contrast, electron transfer involving the 3+/2+ redox couple is only operative in a particular sub-family of these proteins called the high-potential iron–sulfur proteins (HiPIP in short). One component only, corresponding to four equivalent iron ions with $\delta\approx0.45$ mm s^{-1}, is seen by Mössbauer in $[4Fe–4S^*]^{2+}$, a value which appears as an average of that for the ferric and ferrous ions. This observation exemplifies *valence delocalization* within these 4Fe

clusters, that is the existence of formal $Fe^{2.5+}$–$Fe^{2.5+}$ pairs. This phenomenon is also observed in $[4Fe–4S^*]^{1+/3+}$, where one of the two pairs of iron ions, beside the ferrous ($\delta \approx 0.62$ mm s^{-1}) (resp. ferric: $\delta \approx 0.30$ mm s^{-1}) pair, has $\delta \approx 0.50$ mm s^{-1} in $[4Fe–4S^*]^{1+}$ and $\delta \approx 0.40$ mm s^{-1} in $[4Fe–4S^*]^{3+}$ [1,10].

In addition, an increasing number of [3Fe–4S*] clusters [Fig. 1(c)] have been identified in ferredoxins and other enzymes in recent years. The structure of the cluster is equivalent to that of a [4Fe–4S*] cluster having lost one iron atom. They can in fact, through parallel coupling to an oxidation process, loose or recover reversibly this iron atom. This property seems to play an important role in the corresponding enzymes. The three iron ions are ferric in oxidized $[3Fe–4S^*]^{1+}$ ($\delta \approx 0.27$ mm s^{-1}) clusters [11] whereas the reduced $[3Fe–4S^*]^{0}$ clusters present one ferric component ($\delta \approx 0.32$ mm s^{-1}) and a delocalized mixed-valence pair ($\delta \approx 0.45$ mm s^{-1}) [10].

To sum up as this stage of the discussion, ferric ions in such a (roughly) tetrahedral sulfur environment are always found to be high spin ($S = 5/2$) with a typical ferric isomer shift range spread within the limits [0.25–0.32] mm s^{-1}, and a similar correlation can be established between isomer shifts and the ferrous redox state, with a typical range for δ of [0.62–0.72] mm s^{-1}. Mixed-valence ions are, therefore, found in the range [0.40–0.50] mm s^{-1} (see Table 1). We may also notice in passing that another Mössbauer parameter, probing this time the distribution of the charge density around the iron nucleus, is the quadrupole splitting ΔE_Q (also expressed in mm s^{-1}). This complementary term to the isomer shift allows further characterization of the valence state of the iron ions, here imbedded in the sulfur ligand field. Its magnitude is thus found to be typically around 0.5–0.7 mm s^{-1} for a ferric ion, around 2.0–3.0 mm s^{-1} for a ferrous ion.

No proper five iron cluster is known, but it is now accepted that some proteins extracted from sulfate reducing bacteria [12,13] have an active site constituted of a [6Fe–6S*] active site with a structure (most probably) similar to that represented in Fig. 1(e).

Finally, the nitrogenase enzyme which ensures nitrogen fixation in the biosphere, contains two types of active site clusters of intringuing character. One of them, represented in Fig. 1(f) and called "center P", is a [8Fe–8S*] cluster corresponding to two interconnected [4Fe–4S*] clusters. It serves as a relay for electron transfer towards the final active site where nitrogen fixation and reduction occurs. This second cluster, often called the "MoFe cofactor", contains a molybdenum atom (vanadium or iron in some cases) in addition to the iron and sulfur atoms. Its formula is accordingly [(7Fe,1Mo)–9S*] and is represented in Fig. 1(g). It is quite peculiar since only one iron is externally coordinated to a cystein aminoacid, while the six remaining iron atoms appear to be only tricoordinated.

In this context, it is now necessary to mention the existence of *synthetic complexes* which constitute *accurate analogs* of protein-bound active sites. Once synthetized and characterized, they exhibit the same cluster structure as their natural counterparts, where, of course, thiolate ligands are replaced by cystein ligands. The development of their syntheses and subsequent studies, of fundamental importance as will be illustrated below, is mainly due, in the case of Fe–S clusters, to R. H. Holm and coworkers. During the seventies [1], they began to describe synthetic routes, corre-

sponding to self-assembling processes starting from sulfur, iron chloride and thiolate ligands, leading to these analog iron–sulfur clusters. In this way, they rapidly demonstrated that the iron–sulfur species of iron nuclearities 1, 2 and 4 could be synthesized rather easily, although under strict anaerobic conditions [11,14]. However, those clusters of nuclearity 6 were described later [15], and even more recently in the case of nuclearity 3 [16], which is equivalent to the active site of Fig. 1(c).

Several comments must be made concerning these many structures in proteins and in synthetic compounds. At first, they mainly involve the Fe^{2+} and Fe^{3+} redox states of the iron atoms and, most often, in such a way as to exhibit both of them in what are called *mixed-valence charge states* presenting localized and/or delocalized configurations. Secondly, concerning their role in electron transfer and redox catalysis, one can say that it is easily conceivable that the occurrence of *poly*-metallic active sites can only facilitate electron transfer between them [17]. This is also the case in quite a large number of other metalloproteins which also involve two or more transition metal atoms at their active sites. A third point of interest is that they are modular structures, being able to undergo cluster conversions which, most often, are interconversions of reversible nature (for example $2 \times [2Fe–2S^*] \Leftrightarrow [4Fe–4S^*]$, or $[4Fe–4S^*] \Leftrightarrow [3Fe–4S^*] + Fe$, etc) as is now well established in synthetic models as well as in some categories of Fe–S proteins. This last aspect serves in multipurpose ways: in some instances, a cluster can have one biological function relative to the first form adopted and a seemingly completely different one in its second form[1].

Finally, further Mössbauer studies are generally done (at low temperatures) in varied magnetic fields yielding, for a given cluster, the (isotropic) hyperfine interactions with the ^{57}Fe nucleus at the different iron sites. These measured quantities, generally in combination with EPR studies providing the principal components of the g-tensor of the considered species, allow the value of the total spin of the magnetic ground state to be obtained and finally access to its internal magnetic structure.

Therefore, almost all the iron–sulfur proteins known, as well as the corresponding synthetic analogs modelling their active sites, have been characterized both by Mössbauer [1] and by EPR (see the Table 1 in Ref. [18]). Table 1 presents a summary of these studies, giving the value of total spin in each diverse magnetic ground state, for all the clusters presented in Fig. 1.

3. Contributions of EPR and ENDOR in single crystals to the studies of the [4Fe–4S*] clusters

3.1. Introduction

A common characteristic of the spectroscopic studies evoked above (EPR and Mössbauer) performed on proteins and synthetic models is that they are always carried out in disordered states, i.e. in frozen aqueous solutions for EPR or in polar solvents for Mössbauer. By working under such conditions, much of the available information is lost as nearly all the observables in play within the fabric of these

methods (spectroscopic g-factor, hyperfine and quadrupolar interactions) are described by second rank tensors [19].[1] In a disordered state, the recorded spectra correspond to the summation of singular spectra relative to each of all the orientations taken by the paramagnetic species in the sample. Therefore, they are generally rather broad and badly resolved and it is at best possible to attain, and with mediocre precision, only the principal values of these tensors (called g_1, g_2, g_3 for g-tensors with, by convention, $g_1 > g_2 > g_3$), but not their principal directions (V_1, V_2, V_3). The reader is refered to Ref. [20] for an introduction into the field of molecular magnetism, and to Ref. [21] concerning EPR of exchange coupled systems.

These are among the reasons why we have developed in our laboratory an original approach, leading to detailed studies of the paramagnetic states of the [4Fe–4S*] cubane-analogue clusters. These studies have been performed in single crystals of synthetic analogs. We made the choice of focusing on these clusters primarily because they are the most representative of the whole family, but also because a proper understanding of their magnetic structures in the different oxidation states represents a very significant challenge. In effect, we must deal with a spin system where four high spin iron ions are coupled and where there is, in addition, electron delocalization. These will be illustrated in more detail in Section 6 where we will see that many competing and antagonistic interactions occur within these clusters.

The results of these studies are divided into two parts. The first corresponds to EPR studies of the paramagnetic species and to the corresponding analysis of the observables deduced from these experiments, i.e. their g-tensors. The second corresponds to ENDOR studies devoted to the measurement of tensors of the hyperfine interactions between the electron spin distribution and nuclei having a nuclear spin of 1/2 (^{57}Fe, ^{1}H, ^{13}C), used as probes of this distribution. This mode of presentation is logical as it starts with a global description of the species, given by the g-tensors, to a more detailed one, offering access to the electron spin distribution. This order also naturally results from the fact that Fe and S nuclei are, at natural abundance, essentially ^{56}Fe and ^{32}S which have no nuclear spin.

The EPR spectra show lines whose field variations are only determined by g-anisotropy, without exhibiting any hyperfine interactions. The origin of their linewidths thus depends on the physical state of the sample. In disordered, frozen solution samples, in which state Fe–S proteins and synthetic analogues are usually studied, there are essentially two contributions to the linewidth: firstly, small, unresolved, hyperfine interactions with the protons surrounding the cluster, and secondly, the so-called "g-strain" effect. More explicitly, there are two types of disordered samples. The first one is a powder (i.e. polycristalline samples) ordered at the molecular level but disordered at the macroscopic level. The second one is the amorphous state (i.e. frozen solution samples) disordered at the molecular and

[1] Let us notice here that the g-components are not necessarily those of a tensor in the strict mathematical sense of the term as discussed for example in Section 15.6 of Abragam and Bleaney's book, Electron Paramagnetic Resonance of Transition Ions (Clarendon Press: Oxford, 1970). We will here comply to the usage of the field, as almost all publications on the subject keep speaking of the "tensor" g (as Abragam himself did) or, simply, the g-tensor (as Bleaney did, in the same book). This semantic usage concerns also the hyperfine "tensors".

macroscopic levels. In these two cases, EPR spectra are less resolved that in single crystals due to the summation of spectra corresponding to all molecular orientations. This corresponds to the well known "powder lineshapes" associated for instance with g-anisotropy. The "g-strain" effect is then an additive effect, specific to amorphous samples disordered at the molecular level (i.e. a statistic broadening of each component of the g-tensor arising from the disorder itself).

Generally, in Fe–S clusters, the second contribution dominates the first one, already in X-band spectra, and more so at highier frequencies. By contrast, these effects do not exist in single crystals: EPR studies in single crystals then give much better resolution and permit measurement of all the components (eigenvalues and eigen-directions) of the g-tensors with high precision. However, EPR being a method with relatively low resolution in solids, it is further necessary to call on the electron-nuclear double resonance method called ENDOR (the high-resolution method adjunct to EPR) in order to be able to measure hyperfine tensors since, most often, this last technique results in a substantial gain of resolution of about two orders of magnitude with respect to EPR.

Coming back to [4Fe–4S*] cubane-analogues, Table 1 indicates that the $[4Fe–4S^*]^{2+}$ oxidation state is diamagnetic at low temperatures ($S=0$). By contrast, the ground state of $[4Fe–4S^*]^{3+}$ is found to be equal to $S=1/2$. The situation appears to be more complicated for $[4Fe–4S^*]^{1+}$ since, in proteins as well as in synthetic compounds, the ground state can be either $S=1/2$ or $S=3/2$ depending on small changes of the cubane-analogue geometry and environment [22,23]. In any case, two possibilities are conceivable for single crystal studies by EPR and ENDOR of the paramagnetic states $[4Fe–4S^*]^{3+}$ and $[4Fe–4S^*]^{1+}$. The first consists of studying single crystals of the compound prepared in these states. This has indeed been done in our laboratory by J. and P. Gloux in two different cases corresponding to the same $[4Fe–4S^*]^{1+}$ redox state, one having a $S=1/2$ ground state [24], and the second having a $S=3/2$ ground state [25]. These investigations lead to the full determination of the g-tensors and to their relation to the cubane-analogue geometry. However, this approach relies on the use of pure paramagnetic crystals and, therefore, suffers from the presence of intercluster interactions which not only affect the EPR spectra, but also completely impede the use of ENDOR experiments (this method necessitates conditions where the paramagnetic species is diluted in a diamagnetic matrix).

Therefore, we have developed another approach [26] consisting of irradiating single crystals of model compounds synthesized in their $[4Fe–4S^*]^{2+}$ state with gamma rays. In this way, we indeed observe the simultaneous creation of "oxidized" $[4Fe–4S^*]^{3+}$ and "reduced" $[4Fe–4S^*]^{1+}$ species, both trapped in these crystals and corresponding in a sense to the concomittant trapping of electrons and holes. These species are furthermore oriented and diluted at relatively low concentration in a crystal matrix constituted of diamagnetic $[4Fe–4S^*]^{2+}$ cubane-analogues. The best conditions for high resolution studies by ENDOR experiment are thus restored.

3.2. *Single crystal EPR studies: the g-tensors*

After an initial work on the $(Bu_4N)_2[Fe_4S_4(SC_6H_5)_4]$ compound demonstrating the validity of this approach [26], we performed extensive EPR studies on the

$[4Fe–4S]^{3+}$ and $[4Fe–4S]^{+}$ centers created by gamma irradiation in single crystals of two different compounds: $(Et_4N)_2[Fe_4S_4(SCH_2C_6H_5)_4]$ [27] and $(Et_4N)_2[Fe_4S_4(SC_6H_4\text{-}o\text{-}OH)_4]$ [3]. Both cases are interesting since the first one corresponds to nearly symmetrical cubane-analogues, very close to assuming a D_{2d} symmetry [28] whereas the second one is representative of an asymmetrical cubane-analogue, one iron atom among the four presenting an extra (penta) coordination to the oxygen of the phenol group of its thiolate ligand [29]. Therefore, these two cases serve to illustrate the diverse spectroscopic consequences of more or less symmetric environments on the active site. We can thus directly examine the extent of the electron delocalization process in connection with the equivalence or inequivalence of the iron ions.

As usual in single crystal studies, the tensors are determined from diagrams of the angular variations of the EPR lines in three perpendicular planes, as those reported in Fig. 2, corresponding to the $(Et_4N)_2[Fe_4S_4(SC_6H_4\text{-}o\text{-}OH)_4]$ compound [3]. These variations show that the different paramagnetic centers observed all correspond to $S=1/2$, although with significant g-anisotropy around $g_e=2.0023$ (the free electron value). They can be identified, respectively, with $[4Fe–4S]^{3+}$ and $[4Fe–4S]^{+}$ centers primarily by their shape and their average g value $g_{av}=(g_1+g_2+g_3)/3$. In effect, while the $[4Fe–4S]^{3+}$ state exhibits relatively axial g-tensors with $g_{av}>g_e$ (as for holes in solid-state physics), the $[4Fe–4]^{1+}$ state is characterized by rhombic g-tensors with $g_{av}<g_e$ (as for trapped electrons in solid-state physics). These features are general: they are ascertained empirically in all 4Fe–4S proteins known (see the Table 1 in Ref. [18]) and they are justified theoretically [3] (see also Section 3.3 later).

There is, however, a striking feature, common to all the irradiated crystals of [4Fe–4S*] compounds that we have studied so far, which is well illustrated in Fig. 2. We observe in fact many lines, much more than expected for only one $[4Fe–4S]^{3+}$ and one $[4Fe–4S]^{+}$ center. The analysis of the tensors, calculated from the angular variations of all these lines show that this diversity corresponds in fact to the presence of several $[4Fe–4S]^{3+}$ and $[4Fe–4S]^{+}$ centers differing essentially by the principal directions of their g-tensors and also, but to a lesser extent, by their principal values. Further analysis of these principal directions with respect to the cubane-analogue geometry has allowed us to establish that the principal direction associated with the greatest principal value g_1 lies near the direction of the common perpendicular to the directions of the mixed-valence and ferric–ferrous pairs of iron atoms. Finally, the comparison of these directions for the different centers yields a rather simple explanation of their number and diversity, which is in fact due to the different possibilities that the mixed-valence pair $Fe^{2.5+}$–$Fe^{2.5+}$ has to be localized on two of the four iron atoms of the cubane-analogue cluster.

Firstly, this interpretation has been empirically established from the analysis of our experimental results [27]. Secondly, we proposed very recently, on theoretical grounds, a general model for the interpretation of the principal values and the principal directions of the g-tensors of $[4Fe–4S]^{3+}$ and $[4Fe–4S]^{+}$ centers [3], based on simple qualitative arguments and developed for symmetric compounds of C_{2v} electronic structure. The model thus built allows us to rationalize most of our

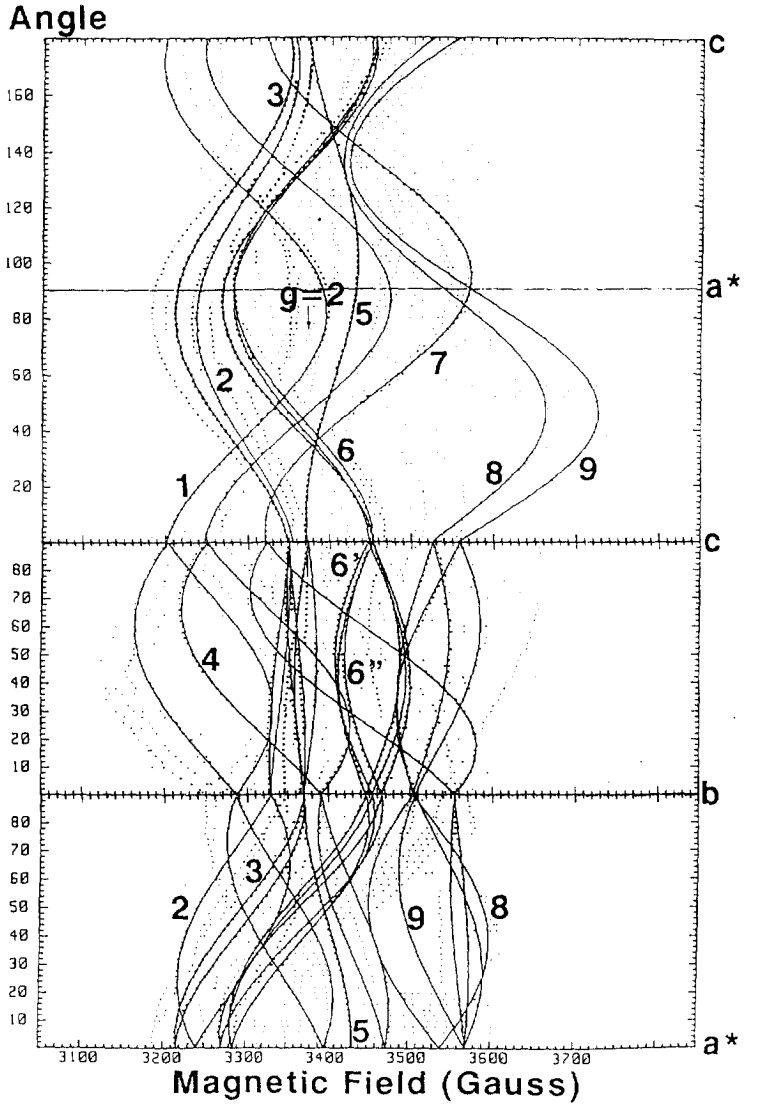

Fig. 2. Angular dependences in the three orthogonal planes a^*b, bc, and ca^* of the EPR lines corresponding to different $[4Fe\text{–}4S]^{3+}$ and $[4Fe\text{–}4S]^{+}$ centers. The continuous curves represent computer fits.

previous results obtained for single crystals of the $(Bu_4N)_2[Fe_4S_4(SC_6H_5)_4]$, $(Et_4N)_2[Fe_4S_4(SCH_2C_6H_5)_4]$ and $(Et_4N)_2[Fe_4S_4(SC_6H_4\text{-}o\text{-}OH)_4]$ compounds. It explains the correlation existing between the location of the mixed-valence pair in the cubane-analogue cluster and the principal direction V_1 corresponding to the largest principal value g_1 of the g-tensor. It also shows that the two other eigenvalues of the g-tensor, g_2 and g_3, are expected to have their corresponding principal

directions V_2 and V_3 aligned with the two pairs of identical iron ions. The consequences on the principal directions of the g-tensors produced by the introduction of some asymmetry have been examined for both the $[4Fe–4S]^{3+}$ and $[4Fe–4S]^{+}$ redox states. They appear fairly different in the two cases. We can state that, by taking into account the principal direction V_1 as a valuable tool, we have a useful "rule of thumb" for the determination of the position of the mixed-valence pair for $[4Fe–4S]^{3+}$ centers, despite the fact that we deal here with asymmetric compounds. This conclusion is to be contrasted to what can be deduced for the $[4Fe–4S]^{+}$ states, because of the greater sensitivity of the ferrous ions, main source of g-anisotropy, to their immediate surrounding. In this last case, we think that such a type of correlation still makes good sense for a (nearly) symmetric arrangement in which the two ferrous ions are (nearly) equivalent. However, breaking significantly this mirror-type symmetry within the ferrous pair can lead to unpredictable g-tensor axes.

3.3. Further developments on the g-tensor theory

We will present here a simplified version of a g-tensor model for [4Fe–4S*] clusters. The details have been published elsewhere [3]. We want to focus here more on some insights that can be gained from the analysis of the experimental data in the light of some very simple formulae.

As it turns out, the value of g_{av} (average isotropic part of the g-tensor) is a key factor to identify $[4Fe–4S]^{3+}$ ($g_{av} > g_e$) and $[4Fe–4S]^{+}$ ($g_{av} \leq g_e$) species. Moreover, the three eigenvalues ($g_1 \geq g_2 \geq g_3$) and their corresponding eigenvectors (V_1, V_2, V_3) give some further information about the location of the two pairs of iron ions. In effect, six locations of the mixed-valence pair are possible in principle, but a good correlation between V_1 and the common perpendicular of the two pairs has been empirically established in the case of the $(Et_4N)_2[Fe_4S_4(SCH_2Ph)_4]$ compound (**1**). We will also present and/or discuss data relative to compounds (**2**) $(Bu_4N)_2[Fe_4S_4(SPh)_4]$; and (**3**) $(Et_4N)_2[Fe_4S_4(SC_6H_4\text{-}o\text{-}OH)_4]$.

In order to substantiate this correlation from a theoretical point of view, we calculated site $g_i(Fe^{q+})$-tensors ($q = 2$, 2.5 or 3), using Geurts' procedure [30], which are then combined through spin coupling algebra to yield a total g-tensor for the cluster:

$$g = \sum_{i=1}^{4} K_i g_i(Fe^{q+}), \tag{1}$$

where $K_i = \langle S_{iz} \rangle / \langle S_z \rangle$ stands as the spin projection coefficient of the local spin S_i of the monomer i onto the total spin S of the cluster (with $\sum_i K_i = 1$).

We proceeded further by setting up an analytical model based on a simplified energy level diagram for $[4Fe–4S]^{3+}/[4Fe–4S]^{+}$. Such diagrams have been calculated by density functional theory (DFT) over the years. As far as the main qualitative features are concerned however, they can also be derived from angular overlap arguments (see Fig. 3). The main point is that the ligand levels (here sulfur, with some minor iron content) of both spins are sandwiched between Fe(3d) majority spin (lower) and Fe(3d) minority spin (higher) orbitals ("majority" refers here to

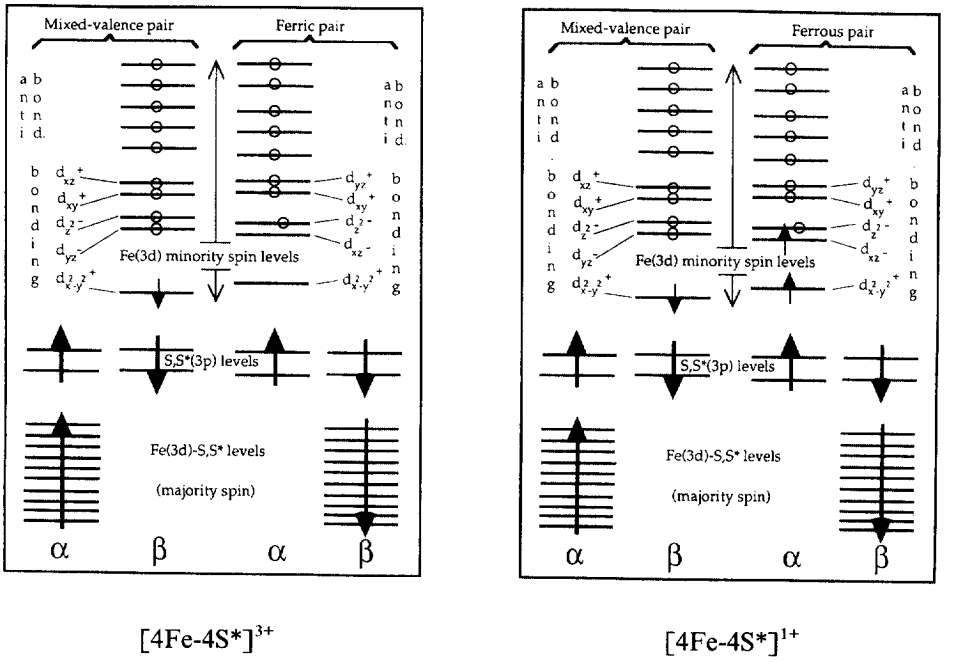

Fig. 3. Full schematic spin-orbital energy diagrams for $[Fe_4S_4(SR)_4]^{1-}$ and $Fe_4S_4(SR)_4]^{3-}$ (OC2 electronic configuration) anions.

the five parallel spins in high-spin iron ions and "minority" to that of the sixth d electron when present). This pattern constitutes the "inverted level scheme". The reference frame is chosen such that x lies along the mixed-valence pair, y along the ferric–ferrous pair, and z along the common perpendicular to both pairs [see Fig. 4(a)].

The (minority spin) metal-ligand antibonding ligand field orbitals form the top set. They can be qualified equivalently as metal–metal bonding and antibonding, and the main transitions responsible for the g-tensor, which will be treated explicitly below, occur among them. Other small contributions come from transitions between the middle (sulfur) set up to the top set, giving rise to a roughly isotropic contribution to the site g_i-tensor called $g(Fe^{q+})$.Id as is known experimentally for the individual ferric ion ($\Delta g(Fe^{3+}) = g(Fe^{3+}) - g_e \approx 0.00$–$0.04$) for which there is no transition within the top set. This contributes also to the mixed-valence and ferrous sites, and we have consequently: $\Delta g(Fe^{2+}) \leq \Delta g(Fe^{2.5+}) \leq \Delta g(Fe^{3+})$.

The components g_{mn} with $\{m, n\} \in \{x, y, z\}$ of a site g_i-tensor will be calculated as following:

$$g_{mn} = g_e + 2\lambda \left(\sum_{\alpha} - \sum_{\beta} \right) \left(\sum_{o} \sum_{p>o} \frac{\langle o|L_m|p\rangle\langle p|L_n|o\rangle}{\epsilon_p - \epsilon_o} \right). \tag{2}$$

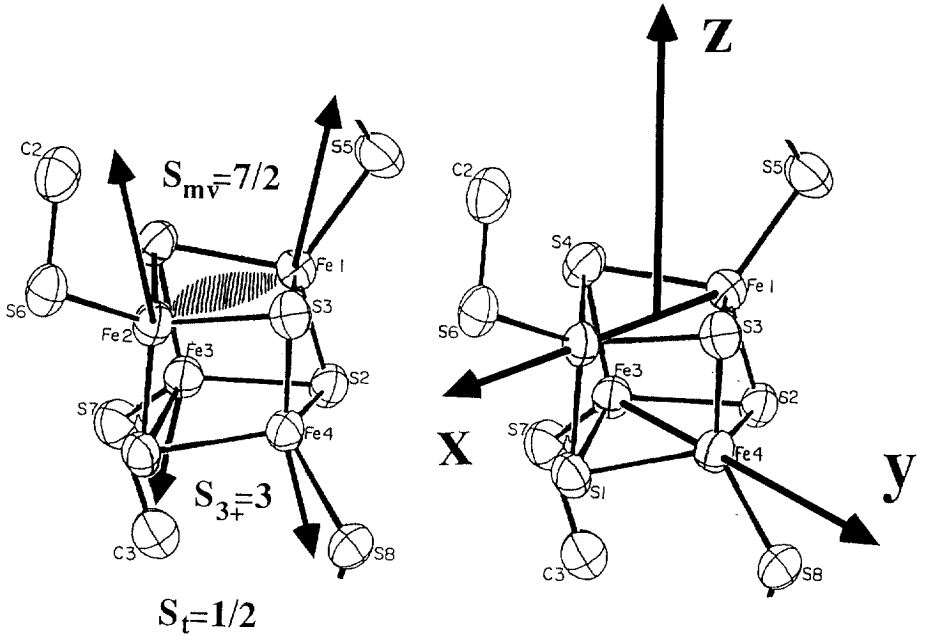

Fig. 4. (Assumed) spin structure for a $[4Fe-4S^*]^{3+}$ center, exhibiting a spin $S_{mv}=7/2$ for its mixed-valence pair, and a spin $S_{3+}=3$ for its ferric pair (a), and corresponding orientation of the (x, y, z) axes, x along the direction of the mixed-valence pair, y along the direction of the ferric pair, and z along the common perpendicular to these two pairs (b).

3.3.1. *case of* $[4Fe-4S^*]^{3+}$

On the mixed-valence pair side, the gap (≥ 0.5 eV) between the occupied $d^+_{x^2-y^2}$ and the three contributing d^+_{xy},d^+_{xz} and d^+_{yz} is large so that we will consider it to first order as a constant: $\Delta\epsilon$. Moreover, roughly the same gap is present in the ferric, mixed-valence, and ferrous pairs: this will further simplify the expressions. On the ferric side, as already mentionned, there is no transition within the top set of iron orbitals. Both mixed-valence and ferric sides, however, exhibit minor contributions originating at the level of the middle sulfur (iron contaminated) orbitals. Therefore, upon using the modes of operation of L_x, L_y and L_z on the real forms of the d-functions, one obtains from Eqs. (1) and (2):

$$\begin{cases} \Delta g_{xx} \approx g_{xx} - g_e \approx \dfrac{\lambda K_{mv}}{\Delta\epsilon} + \Delta g^{ox}_{iso} \\ \Delta g_{yy} \approx g_{yy} - g_e \approx \dfrac{\lambda K_{mv}}{\Delta\epsilon} + \Delta g^{ox}_{iso} \\ \Delta g_{zz} \approx g_{zz} - g_e \approx \dfrac{4\lambda K_{mv}}{\Delta\epsilon} + \Delta g^{ox}_{iso} \end{cases} , \qquad (3)$$

where

$$\Delta g_{iso}^{ox} = [2K_{mv}\Delta g(Fe^{2.5+}) + 2K_{3+}\Delta g(Fe^{3+})]. \quad (4)$$

One notices at first sight that this g-tensor is axial, i.e. $(g_1,\ g_2 \approx g_3) \equiv (g_{zz},\ g_{xx} \approx g_{yy})$, furthermore, with V_1 aligned along the common perpendicular to both iron pairs (the z-axis). These results have already been verified experimentally, for example in a previous study of the nearly symmetric compound $(Et_4N)_2[Fe_4S_4(SCH_2Ph)_4]$. It holds true within a 20° dispersion of the angle values between V_1 and the perpendicular axis to the two pairs. Similar results can be observed for compounds (**2**) and (**3**). This is summarized in Table 2.

Moreover, V_2 and V_3 are aligned with the directions of the ferric and mixed-valence pairs (or vice versa: it depends on the relative ordering of d_{xz}^{+} and d_{yz}^{+} when this small splitting is taken into account). We therefore reported in Table 2 the comparison of the cosines of the Fe–Fe directions in the crystallographic basis (a, b, c^*) of the eigenvectors V_2 and V_3 (associated with the eigenvalues g_2 and g_3) of the g-tensors determined for the oxidized 3+ species of the same compound. Notice that V_2 is systematically aligned with the direction of the ferric pair for centers of which the two pairs are identified (centers III and IV). By way of contrast, center I presents a poor agreement with the theory (concerning V_2 and V_3) although its g-tensor is clearly rhombic. However, we strongly suspect that its structure in this 3+ state is perturbed as compared with that in the diamagnetic 2+ state of the same compound, according to our preliminary investigations by proton ENDOR, and completed ^{13}C ESEEM-FT studies (where ESEEM- stands for "electron spin echo envelope modulation"), performed on both centers IV and I.

In the case of compound (**1**), and in order to appreciate the origin of the dispersion, we introduced phenomenologically some mixing among the $\{d_{xy},\ d_{xz},\ d_{yz}\}$ orbitals such as to yield non zero off diagonal contributions to the g-tensor expressed in (x, y, z). Changing for example d_{xy} into $\cos\theta\ d_{xy} + \sin\theta\ d_{xz}$ introduces a non-zero yz element. In the case of center IV, for example, and to first order, the axes of the g-tensor of center IV result from a rotation of (V_1, V_2, V_3) around x (// V_3, the direction of the mixed-valence pair) by 17–18°. One would expect, therefore, the xy and xz elements of the g-tensor [expressed in (x, y, z)] to be close to zero in contrast to the yz element. By thus fitting the g-tensor of center IV by an adequate model, one could conclude that a value of $\theta \approx 20°$ was required ($\cos^2\theta \approx 0.88$ and $\sin^2\theta \approx 0.12$).

We can go a step further into our analysis by roughly estimating Δg_{iso}^{ox} in the following manner:

$$\Delta g_{iso}^{ox} \approx (2\Delta g_{xx} + 2\Delta g_{yy} - \Delta g_{zz})/3 \approx 2\Delta g_{av} - \Delta g_1. \quad (5)$$

Upon examining Table 2, one can see that the g-tensors of (**1**) there can be clearly divided into two classes, {I, II, V} on the one hand and {III, IV} on the other hand. Interestingly, the centers of the first class have their pairs in "lateral" positions w.r.t. the compression axis of the cubane-analogue whereas the second ones present "orthogonal" pairs to that very same axis. This compression axis is clearly identifiable

Table 2
g-tensors with average values, eigenvalues and direction cosines compared with Fe–Fe directions (in bold) for oxidized centers corresponding to compound (**1**), $[Fe_4S_4(SCH_2Ph)_4]^{1-}$ (I–V); compound (**2**), $[Fe_4S_4(SPh)_4]^{1-}$ (*B*–*B'*); and compound (**3**), $[Fe_4S_4(SC_6H_4\text{-}o\text{-}OH)_4]^{1-}$ (1–3) anions

no.	g_{av}	g_i-values	Δg_{iso}^{ox}	Angles
I		2.142		9°/**14** × **23**
	2.053	2.013	−0.038	42°/**14**
		2.004		40°/**23**
II		2.146		10°/**14** × **23**
	2.053	2.009	−0.043	12°/**23**
		2.003		16°/**14**
III		2.101		11°/**12** × **34**
	2.054	2.039	≈0.005	8°/**34**
		2.023		8°/**12**
IV		2.070		16°/**12** × **34**
	2.038	2.026	≈0.004	17°/**12**
		2.018		6°/**34**
V		2.135		11°/**13** × **24**
	2.055	2.017	−0.027	11°/**24**
		2.014		11°/**13**
B		2.108		10°/**12** × **34**
	2.034	2.005	−0.043	33°/**12**
		1.988		34°/**34**
B'		2.125		15°/**13** × **24**
	2.036	2.006	−0.055	40°/**24**
		1.978		39°/**13**
1		2.138		03°/**12** × **34**
	2.048	2.028	−0.044	30°/**12**
		1.979		32°/**34**
2		2.100		20°/**14** × **23**
	2.041	2.014	−0.020	42°/**14**
		2.010		36°/**23**
3		2.101		03°/**14** × **23**
	2.038	2.015	−0.026	09°/**14**
		2.000		08°/**23**

as $d(Fe_1\text{–}Fe_2) \approx d(Fe_3\text{–}Fe_4) \approx 2.78$ Å whereas all other four Fe–Fe distances average to 2.73 Å. Alternatively, along that compression axis, $d_{av}(Fe\text{–}S^*) \approx 2.24$ Å (average over four bonds) whereas, orthogonal to it, $d_{av}(Fe\text{–}S^*) \approx 2.31$ Å (average over eight bonds). Moreover, upon examining either the spin densities deduced on the iron

ions by the analysis of the anisotropic parts of CH_2 proton hyperfine tensors, or the ^{57}Fe Mössbauer data available, one concluded that center I most probably corresponds to the spin state $|9/2,4,1/2\rangle$ whereas both centers III and IV are more likely to be described by the state $|7/2,3,1/2\rangle$ [cf Fig. 4(b)]. It seems as if, therefore, there is a correlation between the spin state adopted by the cluster as evidenced by its g-tensor (among other experimental data) on the one hand, and the localization of its mixed valence pair w.r.t. the compression axis on the other hand.

Let us, therefore, consider the two families in more detail by estimating the different contributions to the g-tensor eigenvalues. With $\Delta g^{ox}_{isoIII,IV} \approx 0$, one gets from $\Delta g_2 \approx \Delta g_3 \approx 0.024$ that $\lambda K_{mv}/\Delta\epsilon \approx 0.020$ (and $\Delta g_1 \approx 0.08$, exactly as found, but this "prediction" is a logical outcome of Eq. (5)). Similarly, with $\Delta g^{ox}_{isoI,II,V} \approx -0.036$ in average, one gets from $\Delta g_2 \approx \Delta g_3 \approx 0.008$ that $\lambda K_{mv}/\Delta\epsilon \approx 0.044$ (and $\Delta g_1 \approx 0.14$). Both $\lambda K_{mv}/\Delta\epsilon$ values are different, and the spin coupling by itself is not sufficient to take this into account: the ratio of the $K_{mv}/\Delta\epsilon$ values is $(I/IV) \approx 2.2$ whereas that of the K_{mv}'s is only 1.2. Consequently, for centers III and IV, $K_{mv} = +3/2$, $\lambda/\Delta\epsilon \approx 0.013$ and $\Delta\epsilon \approx 0.74$ eV (with $\lambda \approx 80\ cm^{-1}$) whereas for centers I, II and V, $K_{mv} = +11/6$ and $\lambda/\Delta\epsilon \approx 0.024$, that is $\Delta\epsilon \approx 0.41$ eV. Therefore, the gap $\Delta\epsilon$ seems to be larger for centers III and IV and smaller for centers I,II and V (caution: these estimations of $\Delta\epsilon$ are not to be taken as strictly quantitative because of the rough treatment of the terms involved, for example covalency effects).

The difference in localization of the mixed valence pairs thus translates itself into a difference in the energetic structures as evidenced by the analysis of the experimental g-tensors. This last point can be rationalized in the following way: as the cubane-analogue is compressed, all metal orbitals extended along the z-axis (z^2, xz and yz) raise in energy whereas, to first order, x^2-y^2 and xy (lying in a plane perpendicular to that axis) do not move. Therefore, $\Delta\epsilon \approx \epsilon(d^+_{x^2-y^2} - d^+_{xy,\,xz,\,yz})$ is increased on average.

One can also show, in relation to the preceeding result concerning the difference in energetic gaps, that $\Delta g(Fe^{2.5+})$ and/or $\Delta g(Fe^{3+})$ values must be different for both families. In effect, were both these contributions to Δg^{ox}_{iso} identical for all centers, the difference in Δg^{ox}_{iso} values would have to be ascribed to spin coupling only. With centers I,II and V described by the spin state $|9/2,4,1/2\rangle$ [$K_{mv} = (+11/6)$ and $K_{3+} = (-4/3)$] and centers III and IV by the state $|7/2,3,1/2\rangle$ [$K_{mv} = (+3/2)$ and $K_{3+} = (-1)$, one gets $\Delta g^{ox}_{isoI,II,V} \approx (11/3)\Delta g(Fe^{2.5+}) - (8/3)\Delta g(Fe^{3+})$ and $\Delta g^{ox}_{isoIII,IV} \approx 3\Delta g(Fe^{2.5+}) - 2\Delta g(Fe^{3+}) \approx 0$ (cf Table 2). Indeed, the difference in spin coupling by itself would thus lead to $\Delta g^{ox}_{isoI,II,V} \approx (2/3)[\Delta g(Fe^{2.5+}) - \Delta g(Fe^{3+})] < 0$, as found in Table 2, since $\Delta g(Fe^{2.5+}) < \Delta g(Fe^{3+})$. However, this leads also quantitatively to $\Delta g(Fe^{2.5+}) - \Delta g(Fe^{3+}) \approx -0.05$ and, in conjunction with $\Delta g^{ox}_{isoIII,IV} \approx 0$, to $\Delta g(Fe^{2.5+}) \approx 0.10$ and $\Delta g(Fe^{3+}) \approx 0.15$, both values being much too large! [from $\Delta g(Fe^{3+}) \approx 0.02 \pm 0.02$, one gets for center IV: $\Delta g(Fe^{2.5+}) \approx 0.015 \pm 0.015$, and for center I: $\Delta g(Fe^{2.5+}) \approx 0.005 \pm 0.015$].

Compound (**2**) does not exhibit such a clear compression axis, although there are four "short" Fe–S* distances with $d_{av}(Fe–S^*) \approx 2.26$ Å and eight "long" ones with $d_{av}(Fe–S^*) \approx 2.29$ Å. Moreover, $d_{av}(Fe–Fe) \approx 2.73 \pm 0.02$ Å, close to the short Fe–Fe averaged distance for Fe–Fe in compound (**1**) corresponding to "lateral" centers.

Interestingly, both center B (orthogonal) and B′ (lateral) have negative Δg_{iso}^{ox} values comparable to those of "lateral" centers in compound (**1**). Incidently, for B and B′ centers, $\Delta g_2 \approx \Delta g_3 \approx -0.008$ and $\Delta g_{iso\,B,B'}^{ox} \approx -0.05$ in average, that is $\lambda K_{mv}/\Delta\epsilon \approx 0.041$ (as for centers I, II and V).

3.3.2. case of [4Fe–4S]$^+$*

Above the (occupied) delocalized $d_{x^2-y^2}^{+}$ orbital lie two quasi-degenerate orbitals of respective metal d character: d_{xz}^{-} and $d_{z^2}^{-}$ (separated by $\Delta\omega$). One of these two levels is occupied in a ferrous pair, thus giving rise to two quasi-degenerate electronic configurations called OC1 (d_{xz}^{-} below $d_{z^2}^{-}$) and OC2 ($d_{z^2}^{-}$ below d_{xz}^{-}) and to a major contribution to the *g*-tensor because of the small value of Δw. When one calculates explicitely (see details in Ref. [3]), one obtains the following (here again simplified) expressions:

$$e \quad \begin{cases} \Delta g_{xx}^{OC1} \approx \dfrac{\lambda}{2\Delta\epsilon} + \dfrac{3\lambda K_{2+}}{\Delta\epsilon_{yz}} + \Delta g_{iso}^{rd} \\ \Delta g_{yy}^{OC1} \approx \dfrac{\lambda}{2\Delta\epsilon} + \dfrac{3\lambda K_{2+}}{\Delta\omega} + \Delta g_{iso}^{rd} \\ \Delta g_{zz}^{OC1} \approx \dfrac{2\lambda}{\Delta\epsilon} + \Delta g_{iso}^{rd} \end{cases} \quad \begin{cases} \Delta g_{xx}^{OC2} \approx \dfrac{\lambda}{2\Delta\epsilon} + \dfrac{\lambda K_{2+}}{\Delta\epsilon_{xy}} + \Delta g_{iso}^{rd} \\ \Delta g_{yy}^{OC2} \approx \dfrac{\lambda}{2\Delta\epsilon} + \dfrac{3\lambda K_{2+}}{\Delta\omega} + \Delta g_{iso}^{rd}, \\ \Delta g_{zz}^{OC2} \approx \dfrac{2\lambda}{\Delta\epsilon} + \dfrac{\lambda K_{2+}}{\Delta\epsilon_{yz}} + \Delta g_{iso}^{rd} \end{cases} \tag{6}$$

where

$$\Delta g_{iso}^{rd} = [2K_{mv}\Delta g(Fe^{2.5+}) + 2K_{2+}\Delta g(Fe^{2+})] \geq 0, \tag{7}$$

and

$$\Delta\epsilon_m = \epsilon(d_m^{-}) - \epsilon(d_{z^2}^{-}/d_{xz}^{-}). \tag{8}$$

Clearly, $(g_1, g_2, g_3) \equiv (g_{zz}, g_{xx}, g_{yy})$ for that redox state, for both OC1 and OC2. A first question one may ask is how to differentiate between both electronic configurations. Let us therefore consider center I_R of compound (**1**) (see Table 3). It has its mixed-valence pair located on Fe_1–Fe_2 and most probably corresponds to the spin state $|7/2, 3, 1/2\rangle$ (as the 3+ centers III and IV). Assuming OC1 as the correct configuration, and using the estimation for $\lambda/\Delta\epsilon \approx 0.013$, one gets $\Delta g_{iso}^{rd} \approx 0.015 > 0$ (as expected). Consequently, $\Delta w \approx 0.2$ eV, $\Delta\epsilon_{yz} \approx 0.4$ eV and the gap between $d_{x^2-y^2}^{+}$ and d_{xz}^{-} is therefore of the order of 0.5 eV. Again, these numbers stand as orders of magnitude, not as accurate quantitative values.

On that basis alone, one could further predict for an OC2-type center that: $g_1 \approx 2.02$ and $g_2 \approx 2.00$ ($g_3 < g_e$). That center I_R most probably does not assume such an OC2 electronic structure can be readily deduced from the fact that, in such a case, $\Delta g_1 - \Delta g_2 \approx 3\lambda/2\Delta\epsilon \approx 0.02$: this is evidently not realized for center I_R ($\Delta g_1 - \Delta g_2 \approx 0.09$). This could well describe however center V of compound (**3**) (see Table 3), for which $g_1 = 2.010$, $g_2 = 1.994$ and $g_3 = 1.965$. The OC2 configuration

Table 3
g-tensors with average values, eigenvalues and direction cosines compared with Fe–Fe directions (in bold) for rediced centers corresponding to compound (1) $[Fe_4S_4(SCH_2Ph)_4]^{3-}$ (I_R–II_R), compound (2): $[Fe_4S_4(SPh)_4]^{3-}$ (A), and compound (3) $[Fe_4S_4(SC_6H_4\text{-}o\text{-}OH)_4]^{3-}$ (4–9) anions (for center 8-9, no priviledged Fe–Fe directions could be reasonable selected)

no.	g_{av}	g_i-values	Angles
I_R		2.043	20°/**12** × **34**
	1.954	1.948	49°/**12**
		1.871	46°/**34**
II_R		2.087	6°/**14** × **23**
	1.992	1.971	16°/**14**
		1.917	18°/**23**
A		2.090	5°/**13** × **24**
	1.978	1.968	5°/**24**
		1.877	3°/**13**
4		2.096	32°/**13** × **24**
	2.002	1.974	34°/**24**
		1.937	37°/**13**
5		2.010	11°/**13** × **24**
	1.989	1.994	31°/**24**
		1.965	30°/**13**
6		2.058	08°/**14** × **23**
	1.989	1.976	35°/**23**
		1.933	35°/**14**
7		2.045	18°/**12** × **34**
	1.939	1.888	39°/**12**
		1.884	37°/**34**
8		1.980	
	1.914	1.936	?
		1.825	
9		1.971	
	1.902	1.932	?
		1.801	

seems to represent the exception rather than the rule if one considers the set of experimental g-tensors for the reduced redox state $[4Fe\text{–}4S]^+$.

3.4. *Single crystal endor studies: the hyperfine tensors and the electron spin distribution*

Our first attempt to probe in detail the electron spin distribution inside the cubane-analogue cluster is relied on ^{57}Fe ENDOR spectroscopy, with the aim of measuring

complete ^{57}Fe hyperfine interaction tensors [31]. The choice of this nucleus as a probe was a natural one, since these nuclei belong to the atoms located at the heart of the system and at the origin of the magnetism in the cubane-analogue structure. A study has been performed in single crystals of the $(Et_4N)_2[Fe_4S_4(SCH_2C_6H_5)_4]$ synthetic model compound enriched up to 95% in ^{57}Fe, on the $[4Fe–4S^*]^{3+}$ paramagnetic state (called center IV) giving the most intense EPR spectra after irradiation of the diamagnetic compound [31]. Due to the higher resolution offered by ENDOR in single crystals with respect to Mössbauer, it provided much more precise and complete informations ton this state. The hyperfine tensors itself can be decomposed in two parts: an isotropic scalar one, equal to the third of its trace, and the remaining traceless tensor corresponding to its anisotropic part. Two pairs of ^{57}Fe isotropic couplings of -33.5 and -32.7 MHz on the one hand, and $+19.8$ and $+17.4$ MHz on the other hand, were measured. This confirms, but with much more precision than by Mössbauer, the existence of two pairs of (nearly equivalent) iron atoms. The small inequivalences, within each pair, are due to the fact that there is no crystal symmetry relating them. Moreover their anisotropic parts could be obtained with accuracy (both principal values and principal directions), experimental data which were not accessible by Mössbauer. However, it was not possible at this stage to rationalize them, especially the relative principal directions of the two ferric ions. Therefore, these anisotropic parts could not be used in a straightforward way to acquire more information on the electron spin distribution, contrary to what we first thought. This meant in particular that we were not able to assign each of the above ^{57}Fe couplings to definite iron atoms of the crystallographic structure. These difficulties can be traced back to the importance of orbital contributions (difficult to analyze) of the ^{57}Fe hyperfine interactions, coming in addition to the electron spin–nuclear spin contributions.

In order to avoid such difficulties, it becomes necessary to choose other nuclear probes somewhat more distant from the electron spin population and therefore having significant hyperfine interactions but negligible orbital contributions. In the proteins, this is typically the case for the protons of the CH_2 groups of the cysteins, as ascertained by their hyperfine shifts in NMR (see Refs. [32,33], and references therein) and their dominating contributions to ENDOR spectra [34]. This is why we measured by proton ENDOR the hyperfine tensors of the eight protons belonging to the four CH_2 groups of the thiolate ligands in the same $(Et_4N)_2$ $[Fe_4S_4(SCH_2C_6H_5)_4]$ compound as before. The study was also made on the same $[4Fe–4S^*]^{3+}$ paramagnetic state [35], i.e. center IV, as for the previous ^{57}Fe ENDOR study. The problem, with proton ENDOR, is that we expect a very large number of lines. Since there are in general two distinct magnetic sites in the crytal structure of the chosen compound, this translates into 32 lines coming from these eight protons. Moreover, due to dipolar electron–nuclear spin interactions, many more lines must also arise for different crystal orientations from protons of the ligands or of vicinal counterions which are close to the iron atoms of the paramagnetic cluster, the main bearers of the unpaired spin population. Even with the high-resolution carried by ENDOR, the problem becomes quickly untractable. This is why we

decided to perform these studies in a single crystal of the fully deuterated compound, that was deuterated on the phenyl part of the ligands as well as on the counterions. In spite of this, the ENDOR spectra remain just at the limit of resolution and it is a hard and laborious job to obtain their angular variations in three perpendicular planes as presented in Fig. 5. From the fits of these angular variations based on the classical ENDOR Hamiltonian, hyperfine tensors of the eight protons are obtained which constitute an original, abundant and precise source of information since these protons represent peripheral probes giving eight different points of view on the same spin distribution, each one being mainly sensitive to the spin population born by its closest iron atom. These eight symmetric tensors give 48 independent measurements on this distribution. They were then analyzed separatly in terms of their anisotropic and isotropic parts.

Their anisotropic parts correspond to a total of 40 independent components available to determine this spin distribution. They are only due here to the electron–nuclear spin dipolar interactions. Therefore, the distribution of the unpaired electron spin density on the different iron and sulfur atoms could be deduced with the help of a multicentric point-dipole model, using the distances extracted from the crystallographic structure of the diamagnetic $[4Fe–4S^*]^{2+}$ state. Spin populations were thus

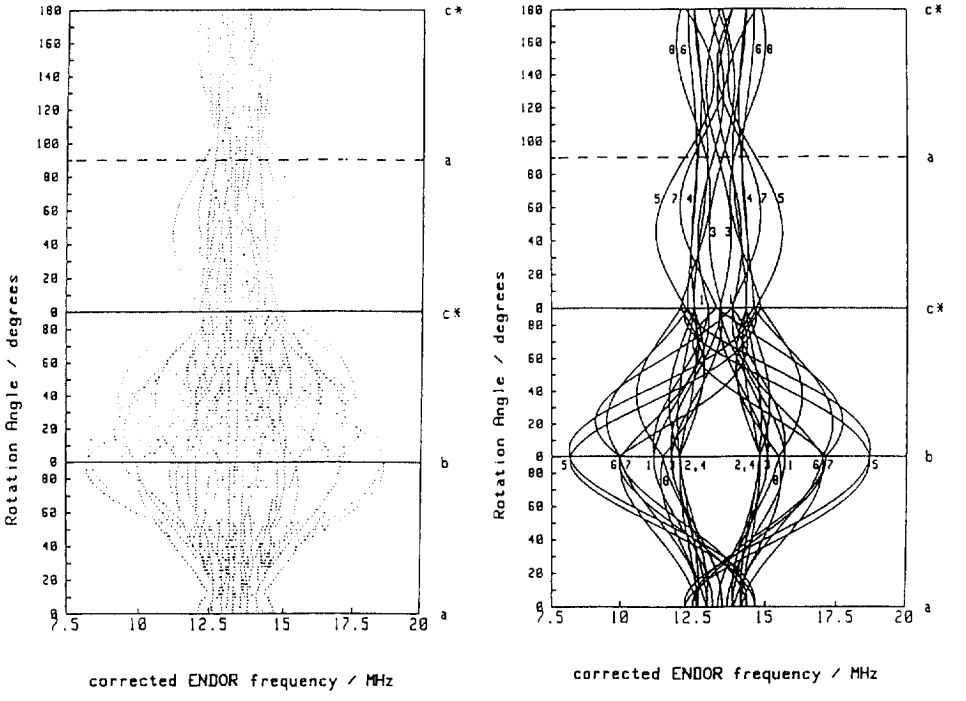

Fig. 5. Angular dependence in the three orthogonal planes *ab*, *bc** and *c*a* of the position of the proton ENDOR lines for the center IV{$[4Fe–4S]^{3+}$ center in compound (**1**)} (left). Fits of the angular dependences of the positions of the same proton ENDOR lines (right).

assigned to each iron atom labelled as in the published crystallographic structure [28]: ≈ -0.7 for Fe_1; ≈ -0.6 for Fe_2; $\approx +1.3$ for Fe_3; and $\approx +1.4$ for Fe_4. The signs and magnitudes of these spin populations allow the non-ambiguous identification of the position of the mixed-valence pair on the two iron atoms Fe_3 and Fe_4 which have the largest and positive spin populations. The spin populations on the irons of the ferric pair are nearly halved and of opposite sign, which immediately indicates an antiferromagnetic order between the magnet moments on the iron atoms on the mixed-valence pair and those on the ferric pair. The spin populations found on the iron atoms can be expressed in terms of a simple and symmetric vectorial spin coupling model [cf Fig. 4(b)] by saying that the magnetic ground state of the species can be best described by a $|7/2,3,1/2\rangle$ ket, where the first number stands for the spin state of the mixed-valence pair, the second one for the spin state of the ferric pair and the last one for the resulting total spin of the cluster. Moreover, minority fractions of the spin population appeared to be delocalized on the organic and inorganic sulfur ligands. They have been found to be of the order of ≈ -0.05 and $+0.04$ for the sulfur of the thiolate ligands, respectively, bound to the irons of the ferric and mixed-valence pairs. For the cubane-analogue inorganic sulfur ions, nearly zero net spin populations were found, but this evaluation is coarse and certainly needs to be better specified in the future. Their small values, certainly smaller than those of found on the sulfur thiolates, result from cancelation effects associated with contributions of opposite signs coming from the positive and negative spin populations of the mixed-valence and ferric pairs.

The measurement of the remaining isotropic parts of the hyperfine interactions $\{A_{iso}(^1H)\}$ of these eight protons of the CH_2 groups of the benzylthiolate ligands stands also per se as a result of great interest. Since each proton tensor has been assigned to a specified CH_2 proton and since the orientation of each CH bond can be defined by a dihedral angle θ with respect to the corresponding Fe–S–C plane from the X-ray structure, we were able to deduce an empirical law concerning these isotropic couplings, as a function of the spin population on the adjacent iron atom (determined previously from the anisotroic tensors) and of the angle θ. It has the general form $A_{iso}(^1H) = D_S(Fe)[A + B\cos\theta + C\cos^2\theta]$. It must be pointed out that this last expression is in good agreement with the one found by I. Bertini and C. Luchinat from NMR studies of oxidized (HiPIP) [4Fe–4S*] proteins, which give the θ dependence of the paramagnetic (hyperfine) shifts of the β-CH_2 groups of the cystein ligands. Therefore, our model seems able to provide the basis for a quantitative interpretation of these shifts in the NMR spectra of proteins. However, we want also to point out that proton hyperfine tensors measured by ENDOR and hyperfine shifts measured by NMR are not fully equivalent. Since ENDOR is performed at low temperatures, between 5 and 10 K, the measured hyperfine tensors are only determined by spin populations in the ground magnetic state. NMR of proteins, however, is made around room temperature and the hyperfine shifts are thus determined both by the spin population of the ground and excited magnetic states populated at this temperature. This is why we are currently developing a new approach based on variable temperature magic-angle solid-state ^{13}C NMR in order to establish precise connections between these two pieces of information.

Continuing along those lines, and after having achieved the first very complete study by ENDOR of a [4Fe–4S*] paramagnetic center, we undertook some further detailed studies, mainly in three different directions:

(1) ^{13}C ESEEM studies[36], by now completed [37], of two $[4Fe–4S^*]^{3+}$ centers (center IV, the same as mentioned earlier, and another oxidized center called I in Ref. [27]) as well as the equivalent study (under way) for the reduced $[4Fe–4S^*]^{1+}$ center I_R in the nomenclature of the same Ref. [27]).

(2) Proton and ^{13}C ENDOR studies of various $[4Fe–4S]^{3+}$ and $[4Fe–4S^*]^{1+}$ centers identified by EPR in single crystals of the same $(Et_4N)_2[Fe_4S_4(SCH_2C_6H_5)_4]$ compound. This illustrates the richness of possibilities that these irradiated crystals offer. However, these studies could not be fully completed until now due to practical limitations coming from the existence of severe overlaps in their EPR and ENDOR spectra and also from problems of sensitivity in ENDOR for those which have not very intense EPR lines. We hope to complete them in the near future by further EPR and ENDOR studies of these centers at Q band.

(3) A first proton ENDOR study [38] of a $[4Fe–4S]^{1+}$ center in the model compound $(Et_4N)_2[Fe_4S_4(SC_6H_4\text{-}o\text{-}OH)_4]$ already evoked above concerning its EPR studies, and which involves an asymmetrical cubane-analogue cluster. There again, and from the study of the angular dependences of the proton ENDOR lines, it has been possible to derive eight hyperfine tensors of protons occupying different positions in the near vicinity of the iron atoms, some of these protons belonging to thiolate ligands of the anion and others to a counter-ion. From the anisotropic parts of the tensors and the multicentric point-dipole model, it has been possible to derive the distribution of the unpaired electron spin population on the different iron (and sulfur) atoms of the cluster, as before. The spin populations obtained indicate that, within the simplifications of the pairwise vectorial spin coupling model, the magnetic ground state corresponds here to a $|9/2, 4, 1/2\rangle$ spin state, where 9/2, 4 and 1/2 are, again, the spin quantum numbers of the mixed-valence pair, of the ferrous pair, and of the whole cluster. Moreover, in this last case, it has been found that the mixed-valence pair is localized , i.e. Fe^{3+}–Fe^{2+}. It is interesting to note the similarities of these results with those known for the reduced aconitase protein from previous Mössbauer and ENDOR measurements [4,38,39].

4. Relation between the hyperfine interactions with ^{57}Fe and the spin densities on the iron atoms

In the previous paragraph concerning the ENDOR studies of the $[4Fe–4S]^{3+}$ center IV, an apparent near proportionality between the ^{57}Fe isotropic hyperfine couplings and the spin populations on the iron ions deduced from the analysis of the anisotropic parts of the proton tensors could be observed. This is why we decided to investigate more precisely this relationship between both quantities and, more specifically, whether a simple proportionnality law were truely adequate. To begin

with, and thus coming back to Mössbauer spectroscopy results, the link between the measured ^{57}Fe isotropic hyperfine parameters $A^{exp}(Fe_i)$ and the spin structure of the magnetic ground state had generally been made in the literature [39] by relying on "universal" or "intrinsic" site values $a(Fe_i)$, defined for rubredoxin-like monomers and supposed to be transferrable to larger clusters through the use of the proportionality relation:

$$A^{exp}(Fe_i) \approx K_i a(Fe_i), \tag{9}$$

where $\{K_i\}$ stand as appropriate spin coupling coefficients translating the way in which local iron spins S_i are projected unto the total spin S of the system (with the normalization relation $\sum_i K_i = 1$):

$$K_i \approx <\mathbf{S}_i \cdot \mathbf{S}> / <\mathbf{S} \cdot \mathbf{S}>. \tag{10}$$

The fact that one defines such a "universal" set of constants $\{a(Fe^{2+}), a(Fe^{2.5+}), a(Fe^{3+})\}$ supposes however that one neglects differential covalent effects among 1Fe, 2Fe, 3Fe and 4Fe clusters, as well as variations in the orbital contributions for "reduced" sites (Fe^{2+} and $Fe^{2.5+}$, as opposed to oxidized Fe^{3+} sites). Those are some of the reasons why we devised a scheme taking into account in an explicit manner covalency factors $d_B(Fe_i)$, defined as the fraction of the iron spin density which remains localized on the metal site and deduced from DFT-based calculations. The factoring out of this effect yields "ionic" quantities $\bar{a}(Fe_i)$:

$$a(Fe_i) = d_B(Fe_i)\bar{a}(Fe_i). \tag{11}$$

These are themselves decomposable into core-polarization (cp) and pseudo-contact (pc) contributions:

$$\bar{a}(Fe_i) = \bar{a}_{cp}(Fe_i) + \bar{a}_{pc}(Fe_i) \tag{12}$$

The first term results from the polarization of the filled s orbitals induced by the net spin of the magnetic orbitals whereas the second one is proportional, first order, to the site $\Delta g(Fe_i)$-tensor of iron (more explicit expressions for both terms are given in Ref. [39]). $\Delta g(Fe_i)$ is related to the total g-tensor of the (paramagnetic) cluster through Eq. (1) in Section 3.3. This whole scheme allowed us to extract proper site values $a(Fe_i)$ for each type of cluster (and iron sites in them) instead of assuming right from the start "universal" values (which they are not anyway). We extracted also by this scheme semi-empirical spin coupling coefficients $K(Fe_i)$ from the experimental measurements $A^{exp}(Fe_i)$ and compared them with theoretical ones calculated for different spin coupling models.

From a practical point of view, the starting point of our analysis was to rely on the fact that $\bar{a}_{pc}(Fe^{3+}) \approx 0$ for ferric ions. Therefore, it is easy to get a transferable value of $\bar{a}_{cp}(Fe^{3+}) \approx -31$ MHz and $K(Fe^{3+})$s from the mean experimental isotropic hyperfine coupling constant of oxidized Rubredoxins and ferric sites of reduced 2Fe ferredoxins. The next logical step yields $\bar{a}_{cp}(Fe^{2.5+}) \approx -32$ MHz and $K(Fe^{2.5+})$'s from the analysis of the available data pertaining to $[3Fe\text{–}4S^*]^0$ and $[4Fe\text{–}4S^*]^{3+}$ clusters containing Fe^{3+} and $Fe^{2.5+}$ ions [see flow charts of the algorithms used for

generating $a(Fe_i)$ and K_i values in Ref. [39]). Finally, since the $[4Fe–4S^*]^{1+}$ clusters are made of formal $Fe^{2.5+}$ and Fe^{2+} ions, we obtained the spin coupling coefficients for that redox state. The same scheme has been applied then to aconitase and $[M–3Fe–4S^*]^{n+}$ clusters (M = V, Co, Ni, Zn and Mo).

Among the main conclusions obtained, let us note that, for HiPIP systems containing $[4Fe–4S^*]^{3+}$ clusters, we found semi-empirically that $K(Fe^{2.5+}) \approx +1.5$ and $K(Fe^{3+}) \approx -1.0$, which are precisely, within a pairwise coupling model, the spin coupling coefficients of the spin state $|7/2, 3, 1/2\rangle$. Alternative models, providing other descriptive languages, are of course possible, the main point remaining that the spin densities on the iron atoms are less than those predicted by maximal coupling of the spins within the mixed-valence pair (i.e. 9/2). The same conclusion is arrived at for "classical" ferredoxin-like $[4Fe–4S^*]^{1+}$ clusters, yielding semi-empirical coefficients intermediary between those of the spin states $|7/2, 3, 1/2\rangle$ and $|5/2, 2, 1/2\rangle$ (as predicted, this time). By contrast, aconitase active sites (also of the type $[4Fe–4S^*]^{1+}$) yield coefficients intermediary between those of $|9/2, 4, 1/2\rangle$ and $|7/2, 3, 1/2\rangle$.

5. The models of competing interactions rationalizing the magnetic properties of the $[4Fe–4S^*]^{3+/2+/1+}$ clusters

From the richness of the data gained from the use of the techniques mentionned above (and of others not discussed in this review) and from their analysis has emerged a unifying picture of what are some of the fundamental mechanisms at play in these Fe–S systems. They will now be presented and illustrated by simple examples although, logically, they lie rather at the very foundation of our understanding and interpretation of the measured quantities summed up in Sections 3 and 4.

The issues raised by the magnetism in these systems have been treated in the previous sections in direct relation to the basic and new experimental results presented and discussed. They are peculiarly interesting and challenging because, as it has already appeared, they involve the interplay of several different kinds of competing interactions. In particular, these interactions are all involved in the reduced $[2Fe–2S^*]^{1+}$ cluster and in the [4Fe–4S*] family, the most challenging one in need of a complete understanding. This is why we intend now to present them in this Section. We will discuss here successively the three biologically relevant redox states $[4Fe–4S^*]^{3+/2+/1+}$ since they strongly depend, because of rather small and subtle effects, on their charge states and give rise to very different behaviors depending on the cases. The issues relevant to the [1Fe] rubredoxins and to the [2Fe–2S*] clusters necessary to the presentation will be introduced within that framework.

The [1Fe] rubredoxin active sites can be thought of as the building-blocks of more elaborate Fe–S clusters. In all cases, the weak ligand-field exerted by the cysteines on the metal d orbitals results in high-spin ferrous $[S(Fe^{2+}) = 2]$ and ferric $[S(Fe^{3+}) = 5/2]$ ions.

Upon "merging" two such monomers together (with four 1- thiolate terminal ligands replaced by two 2- inorganic sulfur ions) one gets [2Fe–2S*] dimers in the

biologically relevant form of the $[2Fe–2S^*]^{2+}$ $(2\times Fe^{3+})$ and the $[2Fe–2S^*]^{1+}$ (Fe^{2+}, Fe^{3+}) species. Two type of interaction appear then. The first one (of electrostatic, although non classical, origin) is mediated by the bridged sulfur atoms. It can be formally described as an exchange coupling between the iron spins, represented by a Heisenberg spin hamiltonian of the form $H_J = J\mathbf{S}_a \cdot \mathbf{S}_b$, of corresponding energy $\langle H_J \rangle = E_J(S) = (J/2)S(S+1)$ where $\mathbf{S}(=\mathbf{S}_{ab}) = \mathbf{S}_a + \mathbf{S}_b$. This allows for the existence of low-lying excited states composing a ladder of magnetic levels. This exchange interaction is essentially antiferromagnetic within the iron–sulfur family (with $J_{Fe^{3+}-Fe^{3+}} > J_{Fe^{3+}-Fe^{2+}} > J_{Fe^{2+}-Fe^{2+}}$), thus leading to low total spin systems, as for the ground states of the oxidized $[2Fe–2S^*]^{2+}$ $(S=0)$ and reduced $[2Fe–2S^*]^{1+}$ $(S=1/2)$ species (see Fig. 6 and Table 1). For more than three spins in interaction, however, it may not possible for all spin pairings to be simultaneously antiferromagnetic. This leads to what is called "spin frustration", as exhibited for the tetrahedral topology of the [4Fe–4S*] spins.

The introduction of a second type of interaction became necessary because of the experimental observation of valence delocalization (i.e. $Fe^{2.5+}$–$Fe^{2.5+}$), especially by Mössbauer spectroscopy, first in [4Fe–4S*] clusters [40,41]. But this phenomenon has also been recently observed in the special case of a Cys-to-Ser mutated *Clostridium pasteurianum* [2Fe–2S*] ferredoxin [42,43], although it has been known for a while for other types of iron dimers [44–49].

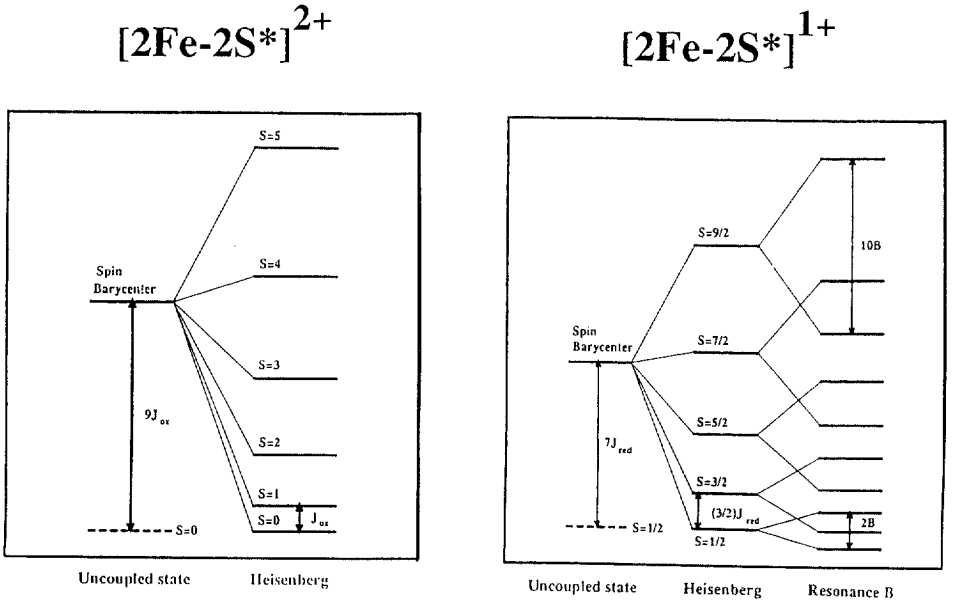

Fig. 6. Heisenberg spin ladder for an oxidized 2Fe2S system, showing the level of the spin barycenter energy (left). Heisenberg spin ladder for a reduced 2Fe2S system, including a resonance *B* term (right) (see text).

The key interpreting concept is that of double-exchange interaction, originating from solid-state physics [50,51], and later introduced in the context of iron–sulfur clusters [52–55]. It is written as $E_B = \pm B(S_{ab} + 1/2)$, where B relates to inter-ion electron transfer. The linear dependence in S_{ab}, spin of the Fe_a–Fe_b dimer, translates the fact that the higher S_{ab} is, the more favorable the interaction will be because of the Pauli exclusion principle (see Fig. 7). The delocalization of the 6th d electron of the ferrous ion "a" to the corresponding empty d orbital of the ferric ion "b" yields a pair of symmetric–antisymmetric wavefunctions $\Psi^{\pm} = 2^{-1/2}(\Psi_a \pm \Psi_b)$ associated with energy levels separated by $2B(S_{ab} + 1/2)$. The magnitude of the parameter B is thus strongly dependent on the overlap $\langle d_a | d_b \rangle \neq 0$.

For such a delocalization process to occur, however, the two iron sites have to be (nearly) energetically equivalent (of class III according to the Robin and Day classification) that is, their ΔE site-energy asymmetry must be sufficiently small. This introduces the concept of charge trapping forces, resulting from vibronic effects, variations in electrostatic environments or in solvent accessibility, etc. These forces tend of course to localize the charges (as does already an antiferromagnetic exchange coupling), which is in contrast to double-exchange mechanisms that favor delocalization.

This competition between antagonistic effects (J, ΔE and B) appears well illustrated in the case of the $[2Fe\text{–}2S^*]^+$ ferredoxin dimer (see Fig. 6, where $\Delta E = 0$ for simplicity). The interplay of these three parameters can be translated into the following eigenvalue problem [48]:

$$\begin{bmatrix} (J/2)S_{ab}(S_{ab}+1) & -B(S_{ab}+1/2) \\ -B(S_{ab}+1/2) & (J/2)S_{ab}+1)-\Delta E \end{bmatrix} \begin{pmatrix} \Psi_a \\ \Psi_b \end{pmatrix} = \epsilon \begin{pmatrix} \Psi_a \\ \Psi_b \end{pmatrix} \tag{13}$$

with eigenfunctions $\Psi^{\pm} = c_a \Psi_a \pm c_b \Psi_b$ where the $\{c_{a,b}\}$ coefficients depend now on the ratio $\Delta E/[B(S_{ab} + 1/2)]$ in such a way that c_a^2 and c_b^2 both tend to 1/2 when $\Delta E/B$

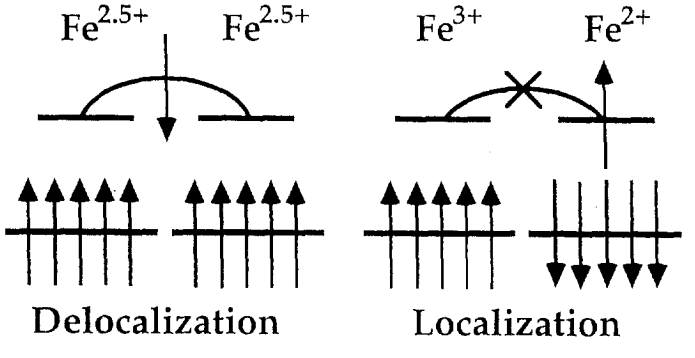

Fig. 7. Dependence of the sixth electron delocalization on ferromagnetic versus antiferromagnetic alignment of the iron spin vectors, due to Pauli exclusion principle. Is shown the occurrence of delocalization with maximal spin for the dimer (left), while a minimal spin results in a valence localized mixed-valence dimer (right).

tend to zero and/or S_{ab} assumes higher values [48] (see Fig. 8). In the case of usual reduced 2Fe ferredoxins however ($S_{ab}=1/2$), a small trapping effect appears sufficient to overcome the delocalization of the ferrous extra electron.

The relative magnitude of J and B has been discussed elsewhere [54,56–67], the consensual picture emerging being that of large (dominating) B terms (up to 900 cm^{-1}) and relatively smaller experimental J values (up to, say, 400 cm^{-1}). A lot of computational effort, especially by using DFT means, has also been done in order to understand both electronic and magnetic structures of these iron–sulfur complexes (Ref. [68], and references therein). Let us now go back to the 4Fe systems, in the light of what we have learned so far from the magnetism of the 2Fe systems.

The $[4Fe–4S^*]^{2+}$ cluster can be seen as resulting from the "merging", in staggered arrangement, of two antiferromagnetically coupled $[2Fe–2S^*]^{2+}$ high-spin dimers [41,60,62,69] in which double-exchange is fully operative. Such a building up of the tetramer explains the experimental observation of four equivalent iron ions of formal charge 2.5+ [40,41] while helping in minimizing the effect of spin frustration. The $[4Fe–4S^*]^{2+}$ has, therefore, a diamagnetic ground state noted $|9/2,9/2,0\rangle$, where the two first numbers refering to the pair spins S_{12} and S_{34} and the last number to its total spin S.

The $[4Fe–4S^*]^{3+}$ state can be best described as made up of a mixed-valence ($Fe^{2.5+}$–$Fe^{2.5+}$) and a ferric (Fe^{3+}–Fe^{3+}) pairs. The ground spin state is always found to be $S=1/2$. The effect of spin frustration is apparent in this 3+ state. In

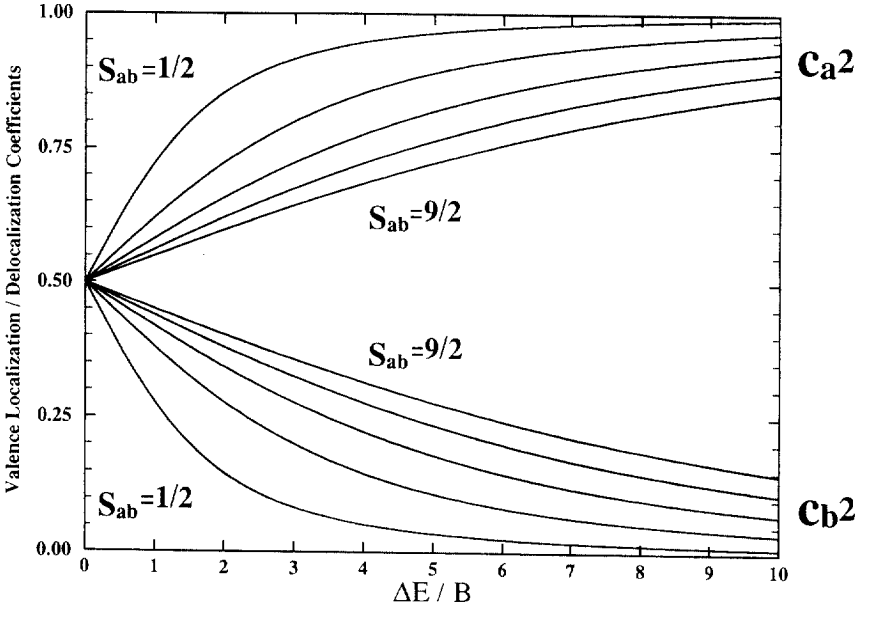

Fig. 8. Squares of the coefficients c_a and c_b in $\Phi=c_a\Phi_a+c_b\Phi b$, solution of the dimer eigenvalue problem including J, B and ΔE (see text). These $\{c_a, c_b\}$ coefficients depend only on the ratio $\Delta E/[B(S_{ab}+1/2)]$ and are shown here for $S_{ab}=1/2$ to 9/2.

effect, the antagonistic satisfaction of stronger exchange coupling between the ferric ions, and weaker inter-pair couplings, results in a non-maximal spin (i.e. 4 instead of 5) at the level of the ferric pair [70,71]. The corresponding ground state is, therefore, $|9/2,4,1/2\rangle$ (or possibly $|7/2,3,1/2\rangle$ [35]).

This cluster is made of a mixed-valence ($Fe^{2.5+}$–$Fe^{2.5+}$) and ferrous (Fe^{2+}–Fe^{2+}) pairs. Spin frustration does not play any significant role here because of weak exchange coupling in the ferrous pair. However, the spin state $|9/2,4,1/2\rangle$ description does not encompass all the experimentally observed ground states, as some have been found to be fully (or nearly so) delocalized $S=3/2$ states. Others stand as physical (or quantum) mixtures of 1/2 and 3/2 states in both natural [72,73] and synthetic [22–25,74] clusters. Rationalizations of that phenomena have been proposed [75–77], the simplest one consisting in invoking a double-exchange B' resonance delocalization ($\sim 600\ cm^{-1}$ computationally [61]) between the high-spin mixed-valence and ferrous pairs [77], in close analogy to what occurs between the high-spin ferric and ferrous ions of the $[2Fe–2S^*]^{1+}$ species with the B term. Such a B' term exists also in $[4Fe–4S^*]^{3+}$ clusters (although of smaller magnitude: $\sim 300\ cm^{-1}$) [61,71], but is fully dominated by larger exchange interaction. In $[4Fe–4S^*]^{1+}$, however, both smaller J's and a larger B' contribute in energetically favoring a $S=3/2$ state as $E(3/2)-E(1/2)=(3/2)J-B'$.

6. Redox potentials of synthetic iron–sulfur clusters: a model

An essential property of many iron–sulfur proteins is that they serve as electron transfer agents. As a consequence, it is of interest to know, in connection with the experimental and theoretical studies (evoked and discussed above) about their electronic and magnetic properties, what are the fundamental contributions determining the relative redox potentials among iron–sulfur active sites, as well as the range of potentials displayed within each family of protein. We want to focus here on the first aspect of the problem and, more specifically, try to understand the relative ordering of the average redox potentials of 1Fe [78], 2Fe [79], 3Fe (both cuboidal [16,80,81] and linear [82–84]), 4Fe [79,85,86] and 6Fe [15] synthetic analogs.

The standard redox potential E^0 is made in general of three contributions:

$$E^0 = IP(\mathrm{rd}) + \Delta E_{\mathrm{PB}} + \Delta SHE, \tag{14}$$

where $IP(\mathrm{rd})$ stands for the gas phase ionization potential $E_{\mathrm{GS}}^{\mathrm{ox}} - E_{\mathrm{GS}}^{\mathrm{rd}}$ for the reduced species, i.e. the difference between the ground state (GS) energies of the oxidized, $E_{\mathrm{GS}}^{\mathrm{ox}}$, and the reduced, $E_{\mathrm{GS}}^{\mathrm{rd}}$, species, ΔE_{PB} stands for the solvation energy difference for the oxidized minus the reduced state, and ΔSHE (≈ -4.5 eV) refers the calculated absolute potential to the standard hydrogen electrode (SHE).

Quantifying these different terms involves the following steps:

(1) calculating the electronic structures and molecular electrostatic potentials for both oxidized and reduced species, for example by DFT means;

(2) deriving sets of charges on the atoms (through a Mulliken analysis, or a least-square fit of the potentials to point charges centered on these atoms);
(3) calculating the solvent reaction field (and subsequent solvation energies) induced by the continuous dielectric medium surrounding the molecules.

The technical aspects related to these different steps have been given elsewhere [61]. But in order to understand what is involved in a simple (or even simplistic) manner, let us construct the following model based on the calculation of redox potentials for Fe–S clusters with S–CH_3 thiolate ligands, i.e. $[Fe_mS_{n-p}(SCH_3)_p]$, made of m iron atoms, $n-p$ inorganic (bridge), and p thiolate (ligand), sulfur atoms (i.e. a total of n sulfur atoms). We will also make a distinction among the actual chemical ligands, dealing separately with alkylthiolate (S-CH_3 = S-R being the prototype) and arylthiolate (S-C_6H_5 = S-Φ being the prototype) ligands as, experimentally,

Table 4
Experimental and best-fit ($E^0_3 - -E^0_{VI}$) redox potentials for synthetic (1–6) Fe–S cluster analogs. Those with alkyl-type ("R") and alryl-type ("Φ") are distinguished, hence the definition of an average E^0_{av}, redox potential for each redox couple

eV units	E°(exp)	E^0_{av}	E^0_{un-av}	E^0_I	E^0_{II}	E^0_{III}	E^0_{IV}	E^0_V	E^0_{VI}
1 $Fe^{1-/2-}$	−0.79(R) (−0.44)	−0.6	≈ −0.6	−0.8	−0.7	−0.7	−0.7	−0.7	−0.7
2 $Fe^{2-/3-}$	−1.25 (R) −0.83 (Φ)	−1.0	≈ −0.8	−1.2	−0.6	−0.7	−0.8	−0.7	−0.6
4 $Fe^{1-/2-}$	+0.18 (R) (+0.53)	+0.4	≈ −0.1	−0.2	+0.0	−0.1	−0.1	−0.1	−0.1
4 $Fe^{2-/3-}$	−1.09 (R) −0.82 (Φ)	−1.0	≈ −0.1	−1.0	−0.3	−0.5	−0.6	−0.5	−0.5
2 $Fe^{3-/4-}$	−1.49 (R) −1.12 (Φ)	−1.3	≈ −1.2	−2.1	(−1.0)	−1.2	−1.4	−1.2	−1.1
3 $Fe^{3-/4-}_L$	−1.49 (R) (−1.14)	−1.3	≈ −1.0	−1.4	(−0.3)	−0.6	−0.7	−0.6	−0.7
3 $Fe^{2-/3-}$	(−0.91) −0.56 (Φ)	−0.7	≈ −0.7	−1.0	(−0.3)	(−0.5)	−0.6	−0.9	−0.9
3 $Fe^{3-/4-}$	(−1.81) −1.46 (Φ)	−1.6	≈ −1.5	−1.8	(−0.6)	(∼0.9)	−1.0	−1.4	−1.4
4 $Fe^{0/1-}$	+0.34[a](R) (+0.69)	+0.5[b]	≈ +0.2	+0.6	(+0.4)	+0.3	+0.4	+0.4	+0.4
4 $Fe^{3-/4-}$	−1.80 (R) −1.50 (Φ)	−1.6	≈ −0.8	−1.8	(−0.7)	−0.9	−1.1	−0.9	−0.9
6 $Fe^{2-/3-}$	(−0.33) +0.02b (Φ)	−0.2	< −0.2	(−0.8)	(−0.1)	(−0.4)	(−0.5)	(−0.3)	(−0.6)
6 $Fe^{3-/4-}$	(−1.15) −0.80b (Φ)	−1.0	> −1.0	(−1.5)	(−0.3)	(−0.7)	(−0.9)	(−0.7)	(+1.1)
rms	—	—	—	0.56	0.17	0.22	0.26	0.20	0.18

[a]Tentatively identified as corresponding to the $4Fe^{0/1-}$ redox couple (see main text).
[b]The actual experimental values (−0.22 and −1.04 wrt SCE, +0.02 and −0.80 wrt SHE) are reported in CH_3CN ($\epsilon = 9$), the calculated one in DMF ($\epsilon = 37$).

there is a systematic shift of 0.3–0.4 eV among the two families (see Table 4). Notice finally that to the $4Fe^{0/1-}$ redox couple is tentatively ascribed the value of +0.34 eV. We will try to see from the calculations below if this identification is plausible or not.

In our analytical model, we plan to focus first on the estimation of the ionization potential (comprising both charge and spin-coupling effects), then on the solvation energy. We will compare our results with DFT-based calculations (as already published elsewhere [61]) and see how to analyze the experimental redox potentials of the 1Fe, 2Fe and 4Fe iron–sulfur cluster families.

6.1. *Estimation of the ionization potential*

By density functional means, we calculated [61] $IP(\mathrm{rd})_{\mathrm{DFT}}$ ionization potentials from spin-coupled ground state energies E_{GS}. If we want to trace back the different contributions to this term $IP(\mathrm{rd})_{\mathrm{DFT}}$, it becomes interesting to refer these same energies E_{GS} to spin-uncoupled states in order to estimate the "weight" of the spin-coupling in redox potentials. Once the effect of the spin-coupling taken into account in a manner described below (see Section 6.2), and removed from calculated or experimental redox potentials, one can estimate the "uncoupled" ionization potential $IP(\mathrm{rd})_{\mathrm{un}}$, of classical electrostatic origin (in contrast with spin-coupling effects of quantum-mechanical electrostatic origin).

We thus need to know the distribution of the charges inside the molecule. Which description of the charge distribution to choose however? Mulliken charges differ substantially from ESP charges (see Table 6 of Ref. [61]) since both are defined for different purposes (fit of the electrostatic potential as far as the latter ones are concerned). We therefore based our estimation of the charges on the fact that "upon reduction, most of the increase in negative charge goes to the S,S* atoms for all FeS clusters considered" [61]. This behavior is related to the "softness" of the sulfur orbitals, and to the relaxation of these orbitals upon oxidation–reduction of the iron–sulfur clusters.

We can thus try to evaluate the relative e–e repulsion energy by first sharing the total anion charge $Q^{\mathrm{ox/rd}}$ among the n sulfur atoms "i" (i.e. $\sum_i q_i^{\mathrm{ox/rd}} = Q^{\mathrm{ox/rd}}$) where q_i stands for the charge of sulfur "i". These q_i's can be seen as spread on the surfaces (or in the volumes: this won't change much the conclusion as will be shown below) of the sulfur ions of radius R_{S} (≈ 1.8 Å) while taking also into account the electrostatic interaction between these charged spheres. For the sake of simplicity, we set: $q^{\mathrm{ox/rd}} = Q^{\mathrm{ox/rd}}/n$, as the iron ions bear almost no net charge: see Table 6 of Ref. [61]) and thus derive charges which are actually very close to Mulliken ones (again, compare Table 5 with Table 6 of Ref. [61] for 4Fe clusters for example). We thus get (up to a constant shift determined through comparison of this model, dealing with part of the charge density, with a full ab-initio type of calculation) a relative ionization potential $\Delta IP(\mathrm{rd})$ expressed as:

$$\Delta IP(\mathrm{rd}) = E_{\mathrm{self}} + E_{\mathrm{pair}}, \tag{15}$$

with:

$$\begin{cases} E_{\text{self}} \approx k\sum_{i}^{n} \dfrac{(q_i^{\text{ox}})2-(q_i^{\text{rd}})^2}{2R_S} \approx \left[\dfrac{k}{n}\right]\dfrac{\Delta Q^2}{2R_S} \\ E_{\text{pair}} \approx k\sum_{i<j}^{n} \dfrac{q_i^{\text{ox}}q_j^{\text{ox}}-q_i^{\text{rd}}q_j^{\text{rd}}}{d_{ij}} \approx \left[\dfrac{k(n-1)}{n}\right]\dfrac{\Delta Q^2}{2d_n} \end{cases}, \tag{16}$$

where $k=14.4$ eV (conversion factor), $\Delta Q^2=(Q^{\text{ox}})^2-(Q^{\text{rd}})^2$ (here $\Delta Q^2<0$), n is the total number of sulfur ions, d_{ij} is the distance between sulfur "i" and sulfur "j", and

$$\sum_{i<j}^{n} \frac{1}{d_{ij}} = \frac{n(n-1)}{2d_n}, \tag{17}$$

thus defining the quantity d_n, which depends on n. One expects d_n to become larger as the cluster size increases, as $1/d_n$ is but an average over the $n(n-1)/2$ inverse distances $\{1/d_{ij}\}$ ($d_4=d_{S-S}$ only for an FeS_4 cluster with tetrahedral arrangement of the sulfur ions). Empirically, $k\,(n-1)/(2nd_n)$ is found to be nearly constant (≈ 1.43) for (1–4)Fe–S clusters[2] (see Table 6: 1.42, 1.45, 1.47, 1.41, 1.44 and 1.37 for 1Fe, 2Fe, 3Fe, $3Fe_L$ [82,83], 4Fe and 6Fe [15] clusters, respectively). For the specific values of n considered here (from 4 to 12), the increase of d_n is partly compensated by that of $(1-1/n)$. In E_{self}, the 1/2 prefactor corresponds to a surface charge-distribution, whereas a 3/5 prefactor corresponds to a uniform enclosed volume for an identically distributed charge. Numerically, $k/(2R_S)\approx 4.0$. The sets of charges that one gets are presented in Table 5 and the resulting self and pair energies in Table 6.

The general trends of the ΔIP(rd) values are as expected: the larger Q and/or the smaller n are, the more negative ΔIP(rd) is. More precisely, from the above formula and for a given $Q^{\text{ox}}/Q^{\text{rd}}$ couple of charges, it is clear that E_{self} will decrease as the number of sulfur atoms increases whereas E_{pair} will be roughly constant because of the prefactor $(n-1)/n$ (compare the E_{self}s and the E_{pair}s within the 1–/2–, 2–/3– and 3–/4– redox couple families).

To compare further our values to density functional results, it is first necessary to correct the calculate results for spin-coupling effects as discussed in the following section.

6.2. Spin coupling effects

The zero point energy reference for spin coupled systems has been defined as the spin barycenter energy E_{BAR} of the spin ladder in order to make visible the stabiliza-

[2] That this last observation is expected to break down for some value of n is clear from the fact that, if taken as rigorously true, it would mean that $d_n \approx 5.0(n-1)/n$, i.e. d_n would be upperbound (which is not the case).

Table 5
Number of sulfur ions (n), total charges for the oxidized (Q_{ox}) and reduced (Q_{rd}) species, as well as corresponding average sulfur charges ($q = Q/n$) used in the model (see main text)

	n	Q_{ox}/Q_{rd}	q_{ox}/q_{rd}
1 $Fe^{1-/2-}$	4	−1/−2	−0.250/−0.500
2 $Fe^{2-/3-}$	6	−2/−3	−0.333/−0.500
4 $Fe^{1-/2-}$	8	−1/−2	−0.125/−0.250
4 $Fe^{1-/3-}$	8	−2/−3	−0.250/−0.375
2 $Fe^{3-/4-}$	6	−3/−4	−0.500/−0.667
3 $Fe_L^{3-/4-}$	8	−3/−4	−0.375/−0.500
3 $Fe^{2-/3-}$	7	−2/−3	−0.286/−0.429
3 $Fe^{3-/4-}$	7	−3/−4	−0.429/−0.571
4 $Fe^{0/1-}$	8	−0/−1	−0.000/−0.125
4 $Fe^{3-/4-}$	8	−3/−4	−0.375/−0.500
6 $Fe^{2-/3-}$	12	−2/−3	−0.250/−0.375
6 $Fe^{3-/4-}$	12	−3/−4	−0.375 −0.500

Table 6
The quantities d_n, E_{self}, E_{pair} and $\Delta IP(rd)$ are defined in the main text

eV units	d_n (Å)	$k\,E_{self}$	$k\,E_{pair}$	$\Delta IP(rd)_{model}$	$IP(rd)_{un\text{-}DFT}$	$IP(rd)_{DFT}$
1 $Fe^{1-/2-}$	3.80	−3.0	−4.2	−7.2 (**0.0**)	1.8(**0.0**)	−1.8
2 $Fe^{2-/3-}$	4.14	−3.3	−7.1	−10.4 (−**3.2**)	−4.9 (−**3.1**)	−5.3
4 $Fe^{1-/2-}$	4.37	−1.5	−4.3	−5.8 (+**1.4**)	$-0.5\ (+\mathbf{1.3}_{\pm 0.3})$	$+0.1_{\pm 0.3}$
4 $Fe^{2-/3-}$	4.37	−2.5	−7.2	−9.7 (−**2.5**)	$-3.6\ (-\mathbf{1.8}_{\pm 0.2})$	$-4.8_{\pm 0.2}$
2 $Fe^{3-/4-}$	4.14	−4.7	−10.1	−14.8 (−7.6)	≈ −9.3 (−7.5)	—
3 $Fe_L^{3-/4-}$	4.47	−3.5	−10.2	−13.7 (−6.5)	≈ −8.2 (−6.4)	—
3 $Fe^{2-/3-}$	4.21	−2.9	−7.3	−10.2 (−3.0)	≈ −4.7 (−2.9)	—
3 $Fe^{3-/4-}$	4.21	−4.0	−10.2	−14.2 (−7.0)	≈ −8.7 (−6.9)	—
4 $Fe^{0/1-}$	4.37	−0.5	−1.4	−1.9 (+5.3)	≈ +3.6 (+5.4)	—
4 $Fe^{3-/4-}$	4.37	−3.5	−10.1	−13.6 (−6.4)	≈ −8.1 (−6.3)	—
6 $Fe^{2-/3-}$	4.82	−1.7	−7.3	−9.0 (−1.8)	≈ −3.5 (−1.7)	—
6 $Fe^{3-/4-}$	4.82	−2.3	−10.2	−12.5 (−5.3)	≈ −7.0 (−5.2)	—

In boldface and/or parentheses are reported relative values (relative to that of the 1Fe redox couple).

tion energy $\Delta E_{BAR} = E_{BAR} - E_{GS}$ gained by "turning on" the coupling. Since $IP(rd) = E_{GS}^{ox} - E_{GS}^{rd}$, one understands that the "turning on" of the coupling will have a contribution to the redox potential of the couple considered, since:

$$\begin{aligned} IP(rd) &= E_{GS}^{ox} - E_{GS}^{rd} \\ &= (E_{BAR} - \Delta E_{BAR})^{ox} - (E_{BAR} - \Delta E_{BAR})^{rd} \\ &= (E_{BAR}^{ox} - E_{BAR}^{rd}) + (\Delta E_{BAR}^{rd} - \Delta E_{BAR}^{ox}) \\ &= IP(rd)_{un} + (\Delta E_{BAR}^{rd} - \Delta E_{BAR}^{ox}). \end{aligned} \tag{18}$$

We make now thus explicit the distinction between spin-coupled [$IP(rd)$] and spin-uncoupled [$IP(rd)_{un}$] ionization potentials. Each ΔE_{BAR} term is made of two

contributions ΔE_{BAR-J} and ΔE_{BAR-B}, due to Heisenberg ($J\sum_{ij}\mathbf{S}_i\cdot\mathbf{S}_j$) and double-exchange ($B$ terms, when present) spin coupling, respectively. With the energy of a Heisenberg spin state of degeneracy $\Delta(S)=2S+1$ written as $E(S)=(J/2)S(S+1)$, and where the double-exchange contribution takes the form $\pm B(S_{ij}+1/2)$ (where the indices "ij" refer to the mixed-valence pair among which electron delocalization may occur), the total spin barycenter stabilization energy can be expressed as [61]:

$$\begin{cases} \Delta E_{BAR-J}=\left\{\dfrac{\sum_{S_{min}}^{S_{max}} D(S)E(S)}{\sum_{S_{min}}^{S_{max}} D(S)}\right\}-E(S_{min}) \\ \Delta E_{BAR-B}=5B \text{ (per delocalised mixed valence pair)} \end{cases} \quad (19)$$

The expression of ΔE_{BAR-J} can be made simpler of course if one defines $E(S)$ in such a way that $\sum_S D(S)E(S)=0$ (for $[2Fe2S]^{2+}$: $E(S)=(J/2)[S(S+1)-S_1(S_1+1)-S_2(S_2+1)]=(J/2)[S(S+1)-35/2]$ for example) in which case $\Delta E_{BAR-J}=-E(S_{min})$ (i.e. $35J/4\approx 9J$ for $[2Fe2S]^{2+}$). As a consequence:

$$\Delta E^{rd}_{BAR}-\Delta E^{ox}_{BAR}=(\Delta E^{rd}_{BAR-J}-\Delta E^{ox}_{BAR-J})+(\Delta E^{rd}_{BAR-B}-\Delta E^{ox}_{BAR-B})$$
$$=\Delta JT+\Delta BT, \quad (20)$$

upon grouping J and B contributions, so that:

$$IP(\mathrm{rd})=IP(\mathrm{rd})_{un}+\Delta JT+\Delta BT. \quad (21)$$

Expressions for ΔJT and ΔBT, as well as average theoretical (DFT-based) values, are given in Table 7, with the disadvantage that these are calculated from overestimated values of spin-coupling terms (as is known for that type of theoretical approach). We will use them to correct the theoretically calculated ground-state energies (as done in Table 6). We propose, however, to use an alternative set of ΔJT and ΔBT terms based on experimentally measured J values (when available), also presented in Table 7, to correct the experimental redox potentials. As can be verified however in Table 7, both theoretical and experiment-based values of $\Delta JT+\Delta BT$ are close within a few tenths of eV for the cases where both data are presented, because of the compensation occuring in ΔJT, sum of positive and negative contributions ($J>0$).

The only marked disagreement between relative values of $IP(\mathrm{rd})_{un}$ and the equivalent DFT-based quantities $IP(\mathrm{rd})_{un\text{-}DFT}$ concerns the $4Fe^{2-/3-}$ redox couple (too negative by 0.7 eV) (see Table 6). This may have two origins. First, we may reach a limit with our simple description of the ionization potential. But why should $4Fe^{2-/3-}$ represent a problem, and not $4Fe^{0/1-}$, $4Fe^{1-/2-}$ (or even $4Fe^{3-/4-}$) if one considers that these two last redox couples behave nicely (see Table 4)? The disagreement might be, however, related to a problem of description of the spin coupling, that is in our theoretical estimation of $\Delta JT+\Delta BT$ (too negative) and, therefore, in that of $IP(\mathrm{rd})_{un\text{-}DFT}$ (consequently too positive). We assumed, as pre-

Table 7
ΔJT and ΔBT estimates according to theoretical J and B values [61], and from experimental ones (when available) that is ($B \approx 800\ cm^{-1} \approx 0.1$ eV)

	ΔJT		ΔBT		$\Delta JT+\Delta BT$ model	$\Delta JT+\Delta BT$ DFT
1 $Fe^{1-/2-}$	—	—	—	—	—	0.0
2 $Fe^{2-/3-}$	$7J_{rd}-9J_{ox}$	≈ -0.2	—	—	≈ -0.2	≈ -0.4
4 $Fe^{1-/2-}$	$25J_{m}-22J_{ox}$	≈ -0.0	$10B_{m}-5B_{ox}$	$\approx +0.5$	$\approx +0.6$	$+0.6$
4 $Fe^{2-/3-}$	$22J_{rd}-25J_{m}$	≈ -0.4	$5B_{rd}-10B_{m}$	≈ -0.5	≈ -0.9	≈ -1.2
2 $Fe^{3-/4-}$	$6J_{s-rd}-7J_{rd}$	≈ -0.1	—	—	≈ -0.1	—
3 $Fe_{L}^{3-/4-}$	$12J_{rd}-15J_{ox}$	≈ -0.3	—	—	≈ -0.3	—
3 $Fe^{2-/3-}$	$14J_{rd}-18J_{ox}$	≈ -0.5	$5B_{rd}$	$\approx +0.5$	$\approx +0.0$	$+0.1$
3 $Fe^{3-/4-}$	$11J_{s-rd}-14J_{d}$	≈ -0.1	$5B_{s-rd}-5B_{rd}$	$\approx +0.0$	≈ -0.1	—
4 $Fe^{0/1-}$	$22J_{ox}-30J_{s-ox}$	≈ -0.2	$5B_{ox}$	$\approx +0.5$	$\approx +0.3$	—
4 $Fe^{3-/4-}$	$20J_{s-rd}-22J_{rd}$	≈ -0.3	$-5B_{rd}$	≈ -0.5	≈ -0.8	—
6 $Fe^{2-/3-}$	?	<0?	$15B_{m}-10B_{ox}$	$\approx +0.5$?	$<+0.5$?	—
6 $Fe^{3-/4-}$	?	<0?	$10B_{rd}-15B_{m}$	≈ -0.5?	<-0.5?	—

For $2Fe^{2-/3-/4-}$, $J_{ox} \approx 350\ cm^{-1}$, $J_{rd} \approx 200\ cm^{-1}$ ($>J_{s-rd}$);
for $3Fe^{2-/3-/4-}$, $J_{ox} \approx 300\ cm^{-1} > J_{rd} \approx 100\ cm^{-1}$ ($>J_{s-rd}$);
for $3Fe_{L}^{3-/4-}$, $J_{ox} \approx 300\ cm^{-1}$ ($J_{rd} \approx 200\ cm^{-1}$);
for $4Fe^{0/1-/2-/3-}$, $J_{s-ox} \approx J_{ox} \approx 400\ cm^{-1}$, $J_{m} \approx 350\ cm^{-1} > J_{rd} \approx 250\ cm^{-1}$ ($>J_{s-rd}$).
For $6Fe^{3-}$, all six iron ions are equivalent, bearing a formal charge of 2.5, hence three assumed mixed-valence pairs, and the lost of one of them by oxidation reduction.

viously [61], that both $[4Fe–4S^*]^{1+}$ and $[4Fe–4S^*]^{3+}$ are described by the spin state $|9/2,4,1/2\rangle$ leading to $\Delta E^{ox/rd}_{BAR-J} = 22\ J_{ox/rd}$ and $\Delta E^{ox/rd}_{BAR-B} = 5\ B_{ox/rd}$, hence the expressions of ΔJT and ΔBT in Table 7 for the two redox couples $4Fe^{1-/2-}$ and $4Fe^{2-/3-}$. Some evidence points to lower values for the pair spins [35,39], resulting in the spin state $|7/2,3,1/2\rangle$ for $[4Fe–4S^*]^{3+}$, or in a mixture of states [75,76] for $[4Fe–4S^*]^{1+}$, but the way in which that would affect our estimations of $\Delta JT+\Delta BT$ is not clear yet (see, however, Section 4.1 of Ref. [61]).

To translate our $IP(rd)_{un}$ into quantities comparable to $IP(rd)_{un\text{-}DFT}$ (thus yielding an absolute scale of the energies), it turns out that we must add an average (empirical) constant shift of $\Delta E_{DFT} \approx 5.5$ eV:

$$IP(rd)_{un} = \Delta IP(rd) + \Delta E_{DFT}. \tag{22}$$

We therefore calculated $IP(rd)_{un}$ for all the other 2Fe, 3Fe, 4Fe and 6Fe redox couples in this way, using Eq. (22) (see Table 6, values in parentheses).

6.3. Solvation energies

Considering now the solvation energies, we will use the rather crude Born model. To first order, the solvation energy, for charged molecules, is determined by the total charge of the anion–cation and by the shape of the molecule: the details of the distribution of the charge inside the molecule among the different atoms intervene as a second-order effet (cf Table 7 of Ref. [61]). Considering a charge Q of a sphere

of radius R with an inside dielectric constant ϵ_{in} imbedded in a continuum solvent of dielectric constant ϵ_{out}, the contribution of the solvation energy to the redox potential is simply expressed as:

$$\Delta E_{PB-model} \approx -k \frac{\Delta Q^2}{2R} \left(\frac{1}{\epsilon_{in}} - \frac{1}{\epsilon_{out}} \right). \tag{23}$$

It remains to evaluate the mean radius of a given cluster. We would like to develop a procedure as simple as possible. For example, we can choose to calculate the volume of a cluster in an approximate way as $V=(4/3)\pi R^3 \approx \sum_i V_i = (4/3)\pi \sum_i R_i^3$, where R_i are the Born radii used in Ref. [61] i.e. $R_{Fe}=1.5$ Å, $R_S=1.8$ Å, $R_C=1.67$ Å and $R_H=1.32$ Å (that is $V_{Fe}\approx 14.1$ Å^3, $V_S\approx 24.4$ Å^3, $V_C\approx 19.5$ Å^3 and $V_H\approx 9.6$ Å^3). Although such an approximation is still acceptable for the inorganic core of the $[Fe_mS_{n-p}]$ cluster, as the contacts between iron and sulfur ions are there essentially ionic ($d_{Fe\text{-}S}\approx 2.3$ Å $\approx R_{Fe}+R_S$), it will tend to overestimate the contribution coming from the (covalent) ligands SCH_3.

Many approximate solutions to that problem are possible. A first one consists in evaluating the total volume of interpenetrating adjacent spheres, one for S, one for C and three for H, with $d_{S\text{-}C}\approx 1.8$ Å and $d_{C\text{-}H}\approx 1.1$ Å. One thus finds that $V_{SCH3}\approx 47$ Å^3. A second one consists in calculating the equivalent radius of the sphere giving rise to the calculated MEAD [88–90] (macroscopic electrostatics with atomic detail) solvation energy for the 1Fe redox couple, i.e. 5.5 eV. One thus gets $R\approx 3.82$ Å and $V_{SCH3}\approx 55$ Å^3 (from $V\approx V_{Fe}+4V_{SCH3}$). Finally, one could optimize V_{Fe}, V_S and V_{SCH3} using the same MEAD solvation energies for 1Fe, 2Fe and (average) 4Fe redox couples. One finds then $V_{Fe}\approx 17$ Å^3, $V_S\approx 27$ Å^3 and $V_{SCH3}\approx 54$ Å^3 (notice the close agreement between these last values of V_{Fe} and V_S and those calculated from Born radii). Upon optimizing rather V_{Fe}, V_S and V_{CH3}, one gets equivalently $V_{Fe}\approx 17$ Å^3, $V_S\approx V_{CH3}\approx 27$ Å^3. We will consider this last set of parameters to evaluate R for the different redox couples. Notice that, in this last approach, no reference is made to interatomic distances, and thus, oxidation–reduction do not affect V (and R).

One obtains for $\Delta E_{PB\text{-}model}$ the estimations presented in Table 8 ($\epsilon_{in}=1$ and $\epsilon_{out}=37$), to be compared with more elaborated results (solving the Poisson–Boltzmann equation with the MEAD code and S–CH_3 ligands).

6.4. Approximate expression for the redox potential

By adding all the approximate expressions for the contributions to the redox potential in iron–sulfur clusters, one obtains:

$$\begin{aligned} E_1^0 &\approx 1.0 + \frac{k\Delta Q^2}{2} \times \left[\frac{1}{nR_S} + \frac{(n-1)}{nd_n} - \frac{1}{R}\left(1 - \frac{1}{\epsilon_{out}}\right) \right] \\ &\approx 1.0 + \Delta Q^2 \times \left[\frac{4.0}{n} + \frac{7.2(n-1)}{nd_n} - \frac{7.2}{R}\left(1 - \frac{1}{\epsilon_{out}}\right) \right], \end{aligned} \tag{24}$$

Table 8
Solvation radii and solvation energies (see main text)

eV units	R (Å)	$\Delta E_{\text{PB-model}}$	$\Delta E_{\text{PB-MEAD}}$
1 $Fe^{1-/2-}$	3.82[a]	+5.5	+5.5
2 $Fe^{2-/3-}$	4.17[a]	+8.4	+8.4
4 $Fe^{1-/2-}$	(4.47[a]) 4.54[b]	+4.6	+4.7
4 $Fe^{2-/3-}$	(4.61[a]) 4.54[b]	+7.7	+7.6
2 $Fe^{3-/4-}$	4.17	+11.7	—
3 $Fe_L^{3-/4-}$	4.47	+11.0	—
3 $Fe^{2-/3-}$	4.25	+8.2	—
3 $Fe^{3-/4-}$	4.25	+11.5	—
4 $Fe^{0/1-}$	4.54	+1.5	—
4 $Fe^{3-/4-}$	4.54	+10.8	—
6 $Fe^{2-/3-}$	5.20	+6.7	—
6 $Fe^{3-/4-}$	5.20	+9.4	

[a]Radii derived from $\Delta E_{\text{PB-MEAD}}$ using Born formula $\Delta E_{\text{PB-model}}$.
[b]Average over the two 4Fe redox couples considered here.

where the first term (1.0 eV) is the sum of ΔE_{DFT} ($\approx +5.5$ eV) and ΔSHE (≈ -4.5 eV) and $k/2=7.2$, a conversion factor. This formula is to be taken as a semi-quantitative expression helpful for determining trends, not for calculating quantitative redox potentials (see first column of the calculated redox potentials in Table 4, yielding a very poor rms value). According to this analytical model, redox couples having similar terms ($Q^{\text{ox/rd}}$, n, R) should have similar redox potentials as is clear from the comparison in Table 4 of the data pertaining to $(2Fe, 3Fe)^{3-/4-}$ or to $(2Fe, 3Fe)^{2-/3-}$ for example. We calculated pseudo-experimental redox potential values for 1Fe, 2Fe, 3Fe and 4Fe clusters by removing the spin-coupling contributions as estimated in Table 7 from the actual experimental data. One can see that, after such a correction, the two redox couples $4Fe^{1-/2-}$ and $4Fe^{2-/3-}$ end up with the same uncoupled redox potential of -0.1 eV: $IP(\text{rd})_{\text{un}}$ and ΔE_{PB} compensate each other [61], such that the difference between the two experimental redox potentials comes from spin coupling.

It is interesting to realize that it is possible to make Eq. (24) more quantitative. In effect, by writing it as:

$$E^0_{\text{II}--\text{V}} \approx A + \Delta Q^2 \times \left[\frac{B}{n} + \frac{7.2(n-1)C}{nd_n} - \frac{D}{R}\right], \tag{25}$$

where the subscripts refer to calculated results (fits) derived from the formula(e) indicated. The coefficients A, B, C and D can be optimized by minimizing the function erf_N defined as:

$$\begin{cases} \text{erf}_N = \sum_{i=1}^{N} \left[E^0_{\text{II}-\text{V}}(A,B,C,D)_i - E^0_{\text{II}-\text{V}}(\text{exp})_i \right]^2 \\ \\ \text{rms}_N = \sqrt{\dfrac{\text{erf}_N}{N}} \end{cases}, \tag{26}$$

Table 9
Best-fit parameters when C (see main text) is constrained to 1.0

	E^0_{I}	E^0_{II}	E^0_{III}	E^0_{IV}	E^0_{V}
A	1.00*	0.57	0.57	0.64	0.60
B	4.00*	4.95	4.21	4.04	4.23
C	1.00*	1.00*	1.00*	1.00*	1.00*
D	7.00*	8.53	7.92	7.68	7.91
r	1.00*	1.00*	1.00*	1.00*	1.04
rms	0.56	0.18	0.23	0.27	0.22
n	10	4	8	10	10

where "i" runs over the N redox couples selected for the procedure. The parameter A allows implicitely for the optimization of ΔE_{DFT} and for that of R_S — which includes the surface-to-volume aspect of charge distribution — whereas the terms C and D scale the intersulfur elestrostatic repulsion and the solvation energy, respectively. From partial derivatives of erf_N with respect to A, B, C and D, one obtains a set of four linear equations with four unknowns (A, B, C, D). The optimized redox potentials for the redox couples listed in the Table 4 are presented in the same table.

Upon fitting the experimental data, we noticed quickly that C and D exhibit linear dependency, such that it was not possible to let both of them vary freely. We therefore constrained either C to 1.0 or D to 7.0 [$\approx 7.2 \times (1 - 1/37)$]. We will discuss below the data obtained for a constrained D value, as there is no essential difference between these and those obtained by constraining C. We reported however in Tables 9 and 10 the values of the parameters in both fitting procedures, which are in fact close enough to the semi-empirical ones of Eq. (24). They are further stable upon varying the number of redox couples included in the fits (from 4 to 10).

We did not include in the fitting procedure the data pertaining to the 6Fe redox couples as the spin algebra is complicated and uncertain at the present time. By considering only the four redox couples studied in Ref. [61] (yielding E^0_{II} in Table 4), one notices that 3Fe data (both cuboidal and linear) are not well reproduced, in contrast with 2Fe and 4Fe data. The predicted redox potentials are too positive by ~ 0.9 eV for $3Fe^{3-/4-}$. However, one predicts $+0.4$ eV for $4Fe^{0/1-}$, which is close to the (tentatively assigned) value of $+0.2$ eV. We thus considered this identification

Table 10
Best-fit parameters when D (see main text) is constrained to 7.0

	E^0_{I}	E^0_{II}	E^0_{III}	E^0_{IV}	E^0_{V}
A	1.00*	0.52	0.55	0.62	0.58
B	4.00*	4.40	3.98	3.92	4.00
C	1.00*	0.80	0.87	0.90	0.87
D	7.00*	7.00*	7.00*	7.00*	7.00*
r	1.00*	1.00*	1.00*	1.00*	1.05
rms	0.56	0.17	0.22	0.26	0.20
n	10	4	8	10	10

as firm, and proceeded further by including this redox couple in the fitting procedure. Finally, the $4Fe^{2-/3-}$ redox couple seems to be somewhat pathological (whatever the fit envisaged), apparently due to a too negative ionization potential (as already seen in Table 6).

Leaving aside the cuboidal 3Fe clusters aside, one obtains E^0_{III} with a slight increase in the rms value (from fit II to fit III). This improves the calculated redox potential for $3Fe_L^{3-/4-}$. The inclusion of the cuboidal 3Fe cluster data in fit IV further increases the rms value (in Table 4, see column E^0_{IV}) by yielding too positive redox potentials. We suspected therefore that the solvation energy contribution might be the culprit as, experimentally, the stabilization of the corresponding models requires bulky tridendate ligands. This would imply a larger value for R than the assumed 4.25 Å. Indeed, upon optimizing it up to $4.25 \times r = 4.42$ Å ($r = 1.04$) only, the results are much better. Notice that the fits III (all data but the cuboidal 3Fe clusters) and V (all data including corrected cuboidal cluster data) yield very similar parameter sets.

We finally tested the relative numerical constancy of the term $k(n-1)/(2nd_n) \approx 1.43$ in average by setting it as a constant C' to be optimized:

$$E^0_{VI} \approx A + \Delta Q^2 \times \left[\frac{B}{n} + C' - \frac{D}{R}\right]. \tag{27}$$

The results are given in Tables 11 and 12. The fits turn out to be as good as those

Table 11
Best-fit parameters when C' (see main text) is constrained to 1.43

	E^0_I	E^0_{II}	E^0_{III}	E^0_{IV}	E^0_V
A	1.00*	0.66	0.58	0.67	0.61
B	4.00*	4.80	4.38	4.12	4.40
C'	1.43*	1.43*	1.43*	1.43*	1.43*
D	7.00*	8.29	7.99	7.64	7.98
r	1.00*	1.00*	1.00*	1.00*	1.06
rms	0.52	0.20.	0.20	0.31	0.19
n	10	4	8	10	10

Table 12
Best-fit parameters when D (see main text) is constrained to 7.0

	E^0_I	E^0_{II}	E^0_{III}	E^0_{IV}	E^0_V
A	1.00*	0.59	0.56	0.65	0.59
B	4.00*	4.36	4.06	4.08	4.09
C'	1.43*	1.18	1.24	1.28	1.24
D	7.00*	7.00*	7.00*	7.00*	7.00*
r	1.00*	1.00*	1.00*	1.00*	1.07
rms	0.52	0.19	0.19	0.30	0.18
n	10	4	8	10	10

taking account d_n explicitely as becomes clear by comparing Tables 9 and 11 on the one hand, and Tables 10 and 12 on the other hand.

As far as 6Fe redox couples are concerned, it is very interesting to obtain "spin-uncoupled" redox potentials which are not far from the experimental ("spin-coupled") values. The difference must be due, in our approach, to spin-coupling. In Table 7, we tentatively assumed that $\Delta JT+\Delta BT \leq +0.5$ eV for $6Fe^{2-/3-}$ and $\Delta JT+\Delta BT \geq +0.5$ eV for $6Fe^{3-/4-}$. We tend to predict indeed a positive value of $\Delta JT+\Delta BT$ in the first case, and a negative one in the second case, from the difference $E^0_{av}-E^0_{III-V}$.

Acknowledgements

Let us here express our thanks and gratitude to all of those who contributed in one way or another to the different works and results presented in this review, first of all to Gerard Rius, Jocelyne Gloux, Pierre Gloux, Laurent Le Pape and Marielle Crozet for their great and direct involvement in the many spectrometric aspects, as well as to Camillo Giori from Parma University (Italy) during his stay in our laboratory in 1991. Louis Noodleman and David Case from the Scripps Research Institute (La Jolla, USA) where one of us (J.-M.M.) spent two years as a post-doc (1992–1993), and, finally, Gerard Desfonds and Gerard L'Hospice for their precious technical assistance.

References

[1] H. Beinert, R.H. Holm, E. Münck, Science 277 (1997) 653–659.
[2] M.K. Johnson, Encyclopedia of Inorganic Chemistry, vol. 4, R.B. King (Ed.), Wiley, Chichester, 1994, pp. 1896–1915.
[3] L. LePape, B. Lamotte, J.-M. Mouesca, G. Rius, J. Am. Chem. Soc. 119 (1997) 9757–9770.
[4] M.M. Werst, M.C. Kennedy, A.L.P. Houseman, H. Beinert, P.M. Hoffman, Biochemistry 29 (1990) 10533.
[5] R.J. Gurbiel, C.J. Batie, M. Sivaraja, A.E. True, J.A. Fee, B.M. Hoffman, D.P. Ballou, Biochemistry 28 (1989) 4861–4871.
[6] C.E. Forde, A.J. Lough, R.H. Morris, R. Ramachandran, Inorg. Chem. 35 (1996) 2747–2751.
[7] C.E. Johnson, J. Phys. (Paris) 35 (C1) (1974) 57–63.
[8] Mixed-Valence Compounds: Theory and Applications in Chemistry, Physics, Geology and Biology, vol. 58, D.B. Brown (Ed.), D. Reidel, Dordrecht, 1980.
[9] Mixed Valency Systems: Applications in Chemistry, Physics and Biology, vol. 343, K. Prassides (Ed.), Kluwer, Dordrecht, 1991.
[10] E. Münck, V. Papaefthymiou, K.K. Surerus, J.-J. Girerd, in: L. Que Jr (Ed.), Metal Clusters in Proteins, vol. 372, American Chemical Society, Washington, DC, 1988, pp. 302–325.
[11] J.M. Berg, R.H. Holm, in: T.G. Spiro (Ed.), Iron–sulfur Proteins, Wiley, New York, 1982, pp. 1–66.
[12] A.J. Pierik, H. Wassink, H. Haaker, W.R. Hagen, Eur. J. Biochem. 206 (1992) 705.
[13] I. Moura, P. Tavares, J.J.G. Moura, N. Ravi, B.H. Huynh, M.-Y. Liu, J. LeGall, J. Biol. Chem. 267 (1992) 4489.
[14] R.H. Holm, Acc. Chem. Res. 16 (1977) 2565.

[15] M.G. Kanatzidis, W.R. Hagen, W.R. Dunham, R.K. Lester, D. Coucouvanis, J. Am. Chem. Soc. 107 (1985) 953–961.
[16] J. Zhou, Z. Hu, E. Münck, R.H. Holm, J. Am. Chem. Soc. 118 (1996) 1966–1980.
[17] E.L. Bominaar, C. Achim, S.A. Borshch, J.-J. Girerd, E. Munck, Inorg. Chem. 36 (1997) 3689–3701.
[18] M. Belinskii, Chem. Phys. 176 (1993) 15–36.
[19] A. Abragam and B. Bleaney, Electron Paramagnetic Resonance of Transition Ions, Clarendon Press, Oxford, 1970.
[20] O. Kahn, Molecular Magnetism, VCH, New York, 1993.
[21] A. Bencini, D. Gatteschi, EPR of Exchange Coupled Systems, Springer, Berlin, 1990.
[22] M.J. Carney, G.C. Papaefthymiou, M.A. Whitener, K. Spartalian, R.B. Frankel, R.H. Holm, Inorg. Chem. 27 (1988) 346–352.
[23] M.J. Carney, G.C. Papaefthymiou, K. Spartalian, R.B. Frankel, R.H. Holm, J. Am. Chem. Soc. 110 (1988) 6084–6095.
[24] J. Gloux, P. Gloux, J. Laugier, J. Am. Chem. Soc. 118 (1996) 11644–11653.
[25] J. Gloux, P. Gloux, J. Am. Chem. Soc. 117 (1995) 7513–7519.
[26] J. Gloux, P. Gloux, B. Lamotte, G. Rius, Phys. Rev. Lett. 54 (1985) 599.
[27] J. Gloux, P. Gloux, B. Lamotte, J.-M. Mouesca, G. Rius, J. Am. Chem. Soc. 116 (1994) 1953–1961.
[28] B.A. Averill, T. Herskovitz, R.H. Holm, J.A. Ibers, J. Am, Chem. Soc. 95 (1973) 3523–3534.
[29] R.E. Johnson, G.C. Papaefthymiou, R.B. Frankel, R.H. Holm, J. Am. Chem. Soc. 105 (1983) 7280–7287.
[30] P.J.M. Geurts, P.C.P. Bouten, A.v.d. Avoird, J. Chem. Phys. 73 (1980) 1306.
[31] G. Rius, B. Lamotte, J. Am. Chem. Soc. 111 (1989) 2464.
[32] I. Bertini, C. Luchinat, NMR of Paramagnetic Substances, Elsevier, Amsterdam, 1996 (Anniversary Volume no. 150).
[33] C. Luchinat, S. Ciurli, in: L.J. Berliner, J. Reuben (Eds.), NMR of Paramagnetic Molecules, vol. 12, chap. 7, New York, 1993, pp. 357–420.
[34] J. Hüttermann, G.P. Däges, H. Reinhard, G. Schmidt, in: G.N. LaMar (Ed.), Nuclear Magnetic Resonance of Paramagnetic Molecules, Vol. NATO ASI Series Vol.457, Kluwer, Amsterdam, 1995, pp. 165–192.
[35] J.-M. Mouesca, G. Rius, B. Lamotte, J. Am. Chem. Soc. 115 (1993) 4714–4731.
[36] M. Crozet, G. Desfonds, B. Lamotte, J.-M. Mouesca, G. Rius, J. Inorg. Biochem. 59 (1995) 357.
[37] M. Crozet, B. Lamotte, J.-M. Mouesca, G. Rius (to be submitted).
[38] L. LePape, B. Lamotte, J.-M. Mouesca, G. Rius, J. Am. Chem. Soc. 119 (1997) 9771–9781.
[39] J.-M. Mouesca, L. Noodleman, D.A. Case, B. Lamotte, Inorg. Chem. 34 (1995) 4347–4359.
[40] D.P.E. Dickson, C.E. Johnson, C.L. Thompson, R. Cammack, M.C.W. Evans, D.O. Hall, K.K. Rao, U. Weser, J. Phys. (Paris) 35 (C6) (1974) 343–346.
[41] P. Middleton, D.P.E. Dickson, C.E. Johnson, J.D. Rush, Eur. J. Biochem. 88 (1978) 135.
[42] B.R. Crouse, J. Meyer, M.K. Johnson, J. Am. Chem. Soc. 117 (1995) 9612–9613.
[43] C. Achim, M.-P. Golinelli, E.L. Bominaar, J. Meyer, E. Münck, J. Am. Chem. Soc. 118 (1996) 8168–8169.
[44] K.K. Surerus, E. Münck, B.S. Snyder, R.H. Holm, J. Am. Chem. Soc. 111 (1989) 5501–5502.
[45] B.S. Snyder, G.S. Patterson, A.J. Abrahamson, R.H. Holm, J. Am. Chem. Soc. 111 (1989) 5214–5223.
[46] S. Drüeke, P. Chaudhuri, K. Pohl, K. Wieghardt, X.-Q. Ding, E. Bill, A. Sawaryn, A.X. Trautwein, H. Winkler, S.J. Gurman, J. Chem. Soc. Chem. Comm. (1989), 59–62.
[47] X.-Q. Ding, E.L. Bominaar, E. Bill, H. Winkler, A.X. Trautwein, S. Drüeke, P. Chaudhuri, K. Wieghardt, J. Chem. Phys. 92 (1990) 178–186.
[48] X.-Q. Ding, E. Bill, A.X. Trautwein, H. Winkler, A. Kostikas, V. Papaefthymiou, A. Simopoulos, P. Beardwood, J.F. Gibson, J. Chem. Phys. 99 (1993) 6421–6428.
[49] D.R. Gamelin, E.L. Bominaar, M.L. Kirk, K. Wieghardt, E.I. Solomon, J. Am. Chem. Soc. 118 (1996) 8085–8097.
[50] C. Zener, Phys. Rev. 82 (1951) 403.
[51] P.W. Anderson, H. Hasegawa, Phys. Rev. 100 (1955) 675.
[52] J.-J. Girerd, J. Chem. Phys. 79 (1983) 1766–1775.

[53] L. Noodleman, E.J. Baerends, J. Am. Chem. Soc. 106 (1984) 2316–2327.
[54] V. Papaefthymiou, J.-J. Girerd, I. Moura, J.J.G. Moura, E. Münck, J. Am. Chem. Soc. 109 (1987) 4703.
[55] G. Blondin, J.-J. Girerd, Chem. Rev. 90 (1990) 1359–1376.
[56] S.F. Sontum, L. Noodleman, D.A. Case, in: D.R. Salahub, M.C. Zerner (Eds.), The Challenge of d and f Electrons: Theory and Computation, American Chemical Society, 1989, pp. 366–377.
[57] L. Noodleman, D.A. Case, S.F. Sontum, J. Chim. Phys. 86 (1989) 743–755.
[58] J. Jordanov, E.K.H. Roth, P.H. Fries, L. Noodleman, Inorg. Chem. 29 (1990) 4288–4292.
[59] S.A. Borshch, E.L. Bominaar, G. Blondin, J.-J. Girerd, J. Am. Chem. Soc. 115 (1993) 5155–5168.
[60] E.L. Bominaar, S.A. Borshch, J.-J. Girerd, J. Am. Chem. Soc. 116 (1994) 5362–5372.
[61] J.-M. Mouesca, J.L. Chen, L. Noodleman, D. Bashford, D.A. Case, J. Am. Chem. Soc. 116 (1994) 11898–11914.
[62] E.L. Bominaar, Z. Hu, E. Münck, J.-J. Girerd, S.A. Borshch, J. Am. Chem. Soc. 117 (1995) 6976–6989.
[63] G. Blondin, J.-J. Girerd, JBIC 1 (1996) 170–172.
[64] M. Kröckel, M. Grodzicki, V. Papaefthymiou, A.X. Trautwein, A. Kostikas, JBIC 1 (1996) 173–176.
[65] L. Noodleman, D.A. Case, J.-M. Mouesca, B. Lamotte, JBIC 1 (1996) 177–182.
[66] I. Bertini, C. Luchinat, JBIC 1 (1996) 183–185.
[67] M.I. Belinsky, JBIC 1 (1996) 186–188.
[68] L. Noodleman, C.Y. Peng, D.A. Case, J.-M. Mouesca, Coord. Chem. Rev. 144 (1995) 199–244.
[69] A. Aizman, D.A. Case, J. Am. Chem. Soc. 104 (1982) 3269–3279.
[70] L. Noodleman, Inorg. Chem. 27 (1988) 3677–3679.
[71] J.-M. Mouesca, L. Noodleman, D.A. Case, Int. J. Quant. Chem.; Q. Biol. Symp. 22 (1995) 95–102.
[72] P.A. Lindahl, E.P. Day, T.A. Kent, W.H. Orme-Johnson, E. Münck, J. Biol. Chem. 260 (1985) 11160.
[73] P. Auric, J. Gaillard, J. Meyer, J.-M. Moulis, Biochem. J. 242 (1987) 525–530.
[74] M.J. Carney, R.H. Holm, G.C. Papaefthymiou, R.B. Frankel, J. Am. Chem. Soc. 108 (1986) 3519–3521.
[75] L. Noodleman, Inorg. Chem. 30 (1991) 246–256.
[76] L. Noodleman, Inorg. Chem. 30 (1991) 256–264.
[77] L. Noodleman, D.A. Case, Adv. Inorg. Chem. 38 (1992) 423–470.
[78] R.W. Lane, J.A. Ibers, R.B. Frankel, R.H. Holm, Proc. Natl Acad. Sci. USA 72 (1975) 2868.
[79] J.J. Mayerle, S.E. Denmark, B.V. DePamphilis, J.A. Ibers, R.H. Holm, J. Am. Chem. Soc. 97 (1975) 1032.
[80] A.L. Macedo, I. Moura, J.J.G. Moura, J. LeGall, B.H. Huynh, Inorg. Chem. 32 (1993) 1101–1105.
[81] E.P. Day, J. Peterson, J.J. Bonvoisin, I. Moura, J.J.G. Moura, J. Biol. Chem. 263 (1988) 3684–3689.
[82] J.-J. Girerd, G.C. Papaefthymiou, A.D. Watson, E. Gamp, K.S. Hagen, N. Edelstein, R.B. Frankel, R.H. Holm, J. Am. Chem. Soc. 106 (1984) 5941–5947.
[83] L. Noodleman, D.A. Case, A. Aizman, J. Am. Chem. Soc. 110 (1988) 1001–1005.
[84] S. Ciurli, S.-B. Yu, R.H. Holm, J. Am. Chem. Soc. 112 (1990) 8169–8171.
[85] B.V. DePamphilis, B.A. Averill, T. Herskovitz, L. Que, R.H. Holm, J. Am. Chem. Soc. 96 (1974) 4159.
[86] P.K. Mascharak, K.S. Hagen, J.T. Spence, R.H. Holm, Inorg. Chim. Acta 80 (1983) 157–170.
[88] C. Lim, D. Bashford, M. Karplus, J. Phys. Chem. 95 (1991) 5610–5620.
[89] D. Bashford, Curr. Op. Struct. Biol. 1 (1991) 175–184.
[90] D. Bashford, K. Gerwert, J. Mol. Biol. 224 (1992) 473–486.